西北工业大学研究生学位论文中期考核表

Northwestern Polytechnical University

Graduate Degree Dissertation Mid-term Evaluation Form

学　　　院　　School of Civil Aviation
School　　<u>School of Civil Aviation</u>

学科、专业　　Aerospace Science and Technology
Discipline / Specialty　　<u>Aerospace Science and Technology</u>

姓　　　名
Name　　<u>DHAKAL AMRIT</u>

学位 级别　　硕士
Degree　　<u>Master</u>

导　　　师　　吴宇
Supervisor　　<u>Wu Yu</u>

论文 题目
Dissertation Title　　<u>States estimation of Lithium-ion battery using data driven methods</u>

考核 时间
Date　　<u>2025/11/20</u>

研 究 生 院

Graduate School

姓名 NAME	DHAKAL AMRIT	学号 STUDENT NO.	2023280024	导师 SUPERVISOR	吴宇
题目来源 Source of the Title	Provincial (autonomous region, municipality directly under the Central Government) projects				
论文题目 Title of Dissertation	States estimation of Lithium-ion battery using data driven methods				

<div align="center">

研究工作进展情况
Progress of Research Work

</div>

一、哪些研究内容已按时或提前完成，主要进展和成果。
　　The research content has been done on time or in advance, and the main progress and results

The research content has been done on time or in advance, and the main progress and results
Thesis progress summary table:

Chapter	Title	Progress
1	Introduction, Background and Literature Review	Completed
2	Brief Overview of Li-ion States Estimation methods	Completed
3	CNN-BiGRU with Temporal Attention for SOH and RUL estimation	Completed
4	IPEformer: a time series transformer for SOH Estimation	Not yet completed
5	Experimental Battery Cycling and Validation on Proprietary Data	Not yet completed
6	Conclusion and Future outlook	After the completion of all

Chapter 1 Introduction

1.1 Research Background and Motivation

　　The global energy shift from fossil fuel to renewable sources of energy is ever growing. Electricity is the purest form of energy. The electrical energy is easy to convert to any other forms of energy without losing its efficiency. Electrical energy is used for everything. From powering our personal computers to controlling temperature of room and many more. At the present time we cannot imagine our future without it [1], [2]. There are two main forms of electrical current. Direct current (DC), electrons flow steadily in one direction, like a river. For example, a battery powered flash light. The energy flows from the battery to the bulb. The main sources of DC are batteries, solar panels, fuel cells etc. In contrast, AC is characterized by electrons that constantly switch direction, and it is the standard form generated by power plants and delivered through our wall outlets due to its efficiency over long distances [3].

　　The critical intersection of these two current types is most evident in modern technologies like electric vehicles (EVs) and renewable energy storage. Since batteries can only store and provide DC power, a complex AC-DC and DC-AC convertor is necessary. During charging, AC power from the grid must be converted to DC to be stored in the battery, either by an onboard charger in the vehicle or an external DC fast charger[4]. During driving, the stored DC power must be converted back into AC to efficiently run the vehicle's electric motor. This entire energy ecosystem-from the grid to the battery and back out to the motor-hinges on the health, safety, and efficiency of the battery itself. This is where the Battery Management System (BMS) becomes indispensable. The complexity of a BMS is defined by the application, service-life, safety and reliability concerns[5], [6].

Traditional battery chemistries such as lead-acid type battery does not require complex BMS, whereas LiBs must be protected with application wise complex BMS[7]. LiBs are at the center of attention due to their capability to store more energy in limited space in other words highly energy dense[8]. This means LiBs can also be considered as high-performance device that requires monitoring and safe operating conditions[9]. Unlike more forgiving technologies, they are susceptible to stress, degradation, and even thermal runaway if operated outside their strict operating conditions[10]. For instance, overcharging a LiBs by even a small margin can cause permanent damage and create internal short circuits, while discharging it too deeply can irreversibly degrade its capacity[11], [12], [13]. Furthermore, due to tiny manufacturing variations, the thousands of individual cells in a large pack will naturally charge and discharge at slightly different rates, leading to imbalances that reduce total capacity and strain weaker cells[14], [15]. This demanding characteristic of LiBs chemistry requires a sophisticated BMS. A comparison of different battery chemistries is as shown in Table 1.

TABLE 1-1 Characteristics comparison of different battery chemistries

Battery Chemistry	Nominal voltage	Life cycles	Energy density	Cost	Safety
Lead-Acid	2.0 V	500 - 1,000	30 - 50	Low	Highly Safe
$LiFePO_4$ (LFP)	3.2 V	3,000 - 6,000	90 - 160	Medium	Safest
$LiCoO_2$ (LCO)	3.6 V	500 - 1,000	150 - 240	High	Low
$Li(NiMnCo)O_2$ (NMC)	3.6 V	1,000 - 2,000	150 - 250	Medium	Medium
$Li(NiCoAl)O_2$ (NCA)	3.6 V	500 - 1,500	200 - 280	High	Low
$LiMnO_4$ (LMO)	3.7 V	500 - 1,500	100 - 150	Medium	Good

From table above we can clearly see that, LiBs are the most economical batteries. LiBs are widely used in many fields, mostly in electric vehicles, aircrafts, potable electronics and energy storage systems. Over the life time of battery usage, the LiBs inevitably faces aging and capacity degradation[16], [17]. The battery experiences lots of degradation phenomenon including internal and external causes. Internal Electrochemical properties, external environmental conditions, external operating conditions, internal electrochemical reactions, internal side reactions are some of these causes for non-linear behavior of battery capacity degradation[18], [19]. This non-linear and multi-phenomenon for degradation causes the safety and reliability concern for the LiBs usage. The BMS is responsible for identifying and evaluating these risks before the disaster happen. Various parameters are used to evaluate and identify degradation behavior occurring inside the battery[20], [21], [22].

1.2 Problem Statement

The useful parameters for PHM of a battery are state of health (SOH) and remaining useful life (RUL). SOH is directly related to how much capacity is available in the battery[23]. Accurate estimation of many battery parameters such as state of charge (SOC), state of power (SOP), state of energy (SOE), RUL depend on SOH estimation[24], [25]. SOH degradation depends on the exploitation of the battery. Usually, SOH is represented in percentage. If a battery is not over-exploited and is in good condition then it's SOH should be higher otherwise SOH will be lower[26]. It is usually considered safe to use until the battery has reached 70% SOH. Accurate SOH calculation gives information on whether the battery has reached its end-of-life (EOL)[21], which is of great importance for safety and useability of this battery[27]. On the other hand, SOH is used to determine whether the battery has fulfilled the expected cycles, which is necessary for recycling and can have great environmental significance[28]. As the battery continue to degrade over time, it is of great importance to accurately estimate its SOH because as the battery ages, it's performance decreases. In addition, internal structure integrity of the battery is also at risk. There is high probability of rapid growth of solid electrolyte interphase (SEI) and dendrites inside the battery[29]. This causes the degradation and deformation of internal structure of

the battery, causing internal short circuit and explosion. This explosion is also known as thermal runaway. Once the fire occurs it's very difficult to control[30].

Many accidents occurred in the past due to thermal runaway has caused damage to human life and properties. Fires caused by lithium-ion batteries have become a growing concern in the aviation industry. Although this Air Busan accident is not yet confirmed what kind failure of LiBs caused it to occur. Passengers and crew of the aircraft confirm that the LiBs found in phones, laptops, and power banks were the main cause of the incident [31].
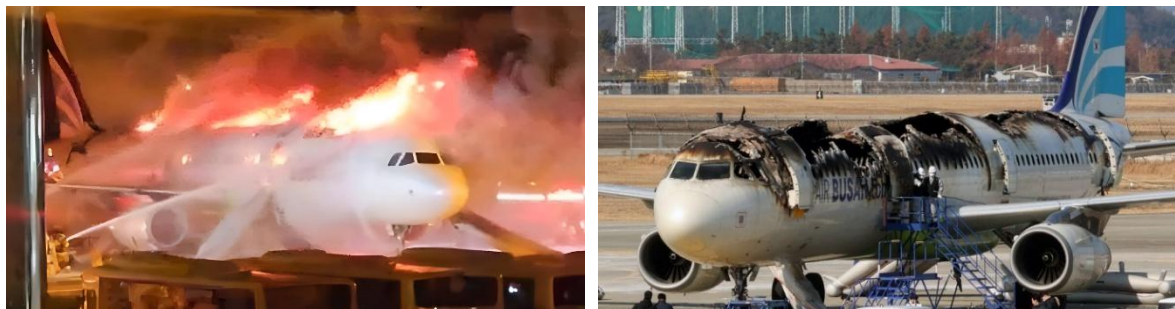

Figure 1-1: Air Busan in South Korea caught fire due to LiBs failure[31]

Similarly, an electric luxury electric car parked in Australia caught fire due to failure of a battery causing the whole battery pack to enter thermal runaway and engulfing nearby cars into the fire[32]. Accidents like these raise safety concern about the use of LiBs.

Figure 1-2: Failure of a LiB used in a luxury car as a energy storage unit caused the fire before spreading to nearby cars. Five cars were destroyed in the fire started from one car's battery failure[32].

LiBs are inherently complex electrochemical systems susceptible to intricate and often irreversible degradation mechanisms, include the growth of SEI layers, lithium plating, and active material loss, which can lead to capacity fade and increased internal resistance. This inherent variability, compounded by the risk of sudden failure, demands a more accurate and reliable estimation of SOH and RUL. RUL is a prognostic metric forecasting the remaining time or cycles until the battery can no longer meet the requirements of its application. The fundamental challenge lies in the fact that the internal degradation processes of LiBs cannot be measured directly during normal operation and are influenced by past usage patterns, environmental conditions, and manufacturing inconsistencies. This inability to precisely pinpoint when a battery will transition from a state of normal aging to a critical failure is a major safety gap. It is precisely this diagnostic and prognostic uncertainty that makes higher-accuracy SOH and RUL estimation a predominant research topic. The ultimate goal is to move from simple estimation methods towards developing intelligent algorithms based on ML and AI that can fuse real-time operational data. These advanced algorithms integrated in BMS provide crucial proactive safety, which are capable of issuing actionable warnings long before a hazardous condition like thermal runaway can occur,

thereby preventing accidents and building essential trust in the technologies that power our future.

1.3 Literature Review of SOH estimation methods

Researcher all over the world are working to find accurate SOH estimation algorithms. Many traditional algorithms use experimental based method to find SOH of a battery[33]. However, these are only applicable in controlled lab conditions and are not accurate enough for real time applications due to the lack of adaptiveness according the degradation condition of the cell. Other algorithms can to divided into two main categories: model-based and data-driven based. Model based algorithms use the detail battery model derived from electrochemical model also known as physics-based model (PBM) or equivalent circuit model (ECM) or electrochemical impedance spectroscopy (EIS) model [7-9]. Physics based methods and EIS are capable of identifying the internal behavior of a cell. The research [37] used EIS with a distribution of relaxation times (DRT) analysis for SOH estimation. DRT was used to deconvolute the EIS data into specific indicators linked to physical degradation modes such as loss of lithium inventory (LLI) and loss of active material (LAM), which were then fed into a piecewise model to predict SOH. Although it links impedance changes directly to the underlying physical and chemical degradation mechanisms inside the cell. However, the methodology relies on laboratory-grade EIS measurements and its need for extensive offline characterization. This limits its immediate practicality, as it requires a significant upgrade to current BMS hardware to implement the precise EIS sensing onboard, and the model must still be generalized for varying SOC and temperatures. . In [38], researchers Presented a novel method for estimating electrode-specific SOH (eSOH) parameters and degradation modes in lithium-ion batteries. The authors used interconnected Sigma-Point Kalman Filters (SPKFs) with a Single-Particle Model with electrolyte dynamics (SPMe) to non-invasively track internal physical degradation, such as loss of active material and lithium inventory, using only standard cell voltage and current measurements. This method provided a deep, physics-based insight into battery aging directly from operational data, enabling more accurate prognostics and facilitating safer, optimized control for applications like electric vehicles and second-life batteries. However, the method's validation is currently limited to simulation, and its real-world performance remains unproven. Physics based methods use the mathematical and physical equations governing the degradation mechanisms inside the cell to determine the aging and estimation SOH. In contrast, machine learning (ML) and deep learning (DL) methods use the charging and discharging data from collected from lab or during the application to estimate the SOH. In paper [39] a Support Vector Regression (SVR) based method was used on NASA dataset for SOH estimation with an differential evolution (DE) optimization algorithm and enhanced health indicators (HI). However, it had high computational complexity due to multi-level optimization involving both DE and modified SVR kernel tuning. In contrast paper [40], focused on computational efficiency by introducing a smoothed SVR method. Using decision tree-based feature selection, it identified key inputs (voltage, discharge time, SOC) and simplified the SVR optimization by transforming the non-differentiable quadratic programming problem into a convex unconstrained minimization problem, solved via conjugate gradient algorithm. This modification reduced training time, though it sacrifices some accuracy compared to standard or DE-optimized SVR. In research [41], the authors proposed an integrated framework combining the Improved Whale Optimization Algorithm (IWOA) with a Variable Forgetting Factor Online Sequential Extreme Learning Machine (VFOS-ELM) and a Particle Filter (PF) for SOH estimation and RUL prediction of LiBs. The VFOS-ELM was used to estimate SOH dynamically, while the IWOA-optimized PF handled RUL prediction. The model employed Extremely Randomized Trees (ERT) for feature selection from voltage, current, temperature, and incremental capacity (IC) data. However, its dependence on high-quality voltage features and sensitivity to initialization parameters in the PF step limit its generalizability. Moreover, the approach requires similar degradation trajectories between training and testing data, restricting applicability. In [42], researchers proposed a hybrid data-driven framework for lithium-ion battery SOH estimation that integrates gradual

decreasing current measurement, double correlation analysis, and a GRU model optimized by the Sparrow Search Algorithm (SSA). The gradual decreasing current from the constant-voltage charging phase was used as raw data, while the double correlation analysis identified combined optimal features containing both relevant and complementary information for SOH characterization. However, it's reliance on charging-phase data limits applicability under partial or irregular charging conditions. Moreover, performance under high-noise environments or limited labeled data remains unverified, suggesting that further validation with more datasets is needed. In [43], the authors presented a CNN whose hyperparameters were optimized via Bayesian optimization to capture complex nonlinear relationships between the raw input signals and battery SOH. It provided a data-driven method that does not rely on manual feature extraction, enabling the model to automatically learn informative patterns directly from raw battery signals. However, the method's reliance on large, high-quality datasets for training may limit its applicability in scenarios with sparse or noisy battery data. In research [44], the authors proposed a CNN-LSTM model enhanced with a Temporal Pattern Attention (TPA) mechanism for estimating the SOH of lithium-ion batteries. The method first applied Local Outlier Factor (LOF) detection and Lagrange interpolation to correct anomalies in health factor data derived from charge–discharge curves. Relevant health factors were then selected using Pearson and Spearman correlation analyses, forming the input dataset for the model. The TPA mechanism was integrated into the CNN-LSTM model to improve its focus on key temporal patterns, while the WOA optimized model hyperparameters to avoid local optima and reduce manual tuning. However, the TPA mechanism increases memory usage and training time, presenting challenges for large-scale or real-time applications.

1.4 Literature review of RUL estimation methods

In [45], researchers proposed an Optimal Deep Belief Network integrated with a Bayesian Algorithm (ODBN-BA) for joint estimation of SOH and RUL in LiBs. The model incorporated Intrinsic Computing Expressive Empirical Mode Decomposition with Adaptive Noise (ICEEMDAN) for comprehensive feature extraction and denoising of complex battery signals. By utilizing the Bayesian Algorithm for parameter tuning, including learning rate, neuron count, and regularization factors, the model achieved improved accuracy, robustness, and generalization compared to conventional methods. The approach was validated on NASA and CALCE battery datasets. However, the ODBN-BA method's computational complexity and limited validation dataset remain unsolved. In [46], researchers presented a comprehensive review of Transformer-based and Artificial General Intelligence (AGI)-driven models for battery state estimation, diagnostics, and lifetime prediction, highlighting a transformative shift from traditional modeling toward data-driven intelligent systems. The paper emphasizes how customized Transformer architectures, originally developed for natural language processing, are repurposed to analyze complex battery time-series data by leveraging self-attention mechanisms that capture intricate temporal dependencies across multiple degradation factors.

The study highlights the collaborative potential between academia and industry, emphasizing that such synergy is vital for translating theoretical advances in Transformer-based diagnostics into commercially viable and scalable solutions for BMS. However, the approach faces several shortcomings. The computational demands of Transformer and AGI models remain a major barrier to deployment in embedded or resource-constrained environments such as BMS. Additionally, theoretical development has outpaced empirical validation; most studies rely on simulation or laboratory datasets rather than real-world, long-term field data. In research [47], researchers proposed a transfer learning-based estimation framework integrating the PatchTST model with a Dynamic Weighted Kernel Mean Square Error (DWKMSE) loss function for the joint prediction of LiBs SOH and RUL. The PatchTST model decomposes battery degradation signals into independent feature channels through channel-agnostic operations, allowing for shared parameter weights and reduced information redundancy. However, the DWKMSE loss introduce higher computational demands, making the approach less

suitable for lightweight embedded BMS without optimization. In [48], researchers proposed an optimized joint estimation framework for State SOH and RUL of LiBs using a hybrid ELM and Relevance Vector Machine (RVM) approach. The authors first extracted relevant electrochemical health features and fed it into ELM model for rapid SOH estimation. The estimated SOH is then used as an input feature for an RVM-based RUL predictor, leveraging the probabilistic nature of RVMs to quantify prediction uncertainty and enhance robustness. However, the dependence on empirical health feature extraction may restrict generalization to batteries with different chemistries or operational profiles.

1.5 Research Objectives and Contributions

The goal of this thesis is to research more accurate SOH and RUL estimation methods based on artificial intelligence (AI). To train such AI models, lots of battery cycling data is necessary. To get the necessary data, many relevant charge-discharge battery cycling experiments are designed. Then the acquired data is splinted into training, testing and validation dataloader then the data is trained using ML and DL frameworks. Finally, developed models are evaluated using different evaluation metrics. Many public datasets are also used to train and test the SOH prediction of proposed methods. The main highlights of this thesis are as follows

- Application of deep neural network (DNN) architecture through integration of CNN-BiGRU and temporal attention for estimating SOH and RUL on CALCE CS2-type battery dataset. The proposed method CNN–BiGRU-Temporal Attention was rigorously compared with other established DL architectures such as CNN, LSTM, CNN-BiLSTM, and BiLSTM-GRU. The proposed model, along with other benchmark models, was evaluated using various metrics such as MAE, RMSE, and R^2.

- Application of IPEformer: Inverted Patch Imbedding Transformer through integration of time series data and DL architectures for battery SOH estimation. The IPEformer was trained and tested with four datasets including, CALCE dataset, NASA dataset, MIT-Stanford dataset, and XJTU dataset. The proposed model is evaluated using evaluation metrics such as MAE, MSE, RMSE, and R^2.

- Battery cycling experiment on cylindrical cells of 2.2 ampere hours (Ah) and pouch cells of 350 milli ampere hours (mAh) capacity is carried out until the cells were fully degraded. A total of 9 cells, 4 cylindrical and 5 pouch cells were used for this experiment. Voltage, current, and temperature of each cell were recorded. The cells were charged and discharged at a room temperature. The room temperature was also recorded for reference.

- The battery cycling experiments performed in length of over six months is used for testing and training the proposed DL based model and is evaluated using evaluation metrics like RMSE, MAE, and R^2.

1.6 Thesis Organization

This thesis is structured to systematically present the research, from foundational knowledge and data acquisition to the development and validation of novel AI models for battery health prognostics. The organization is as follows:

Chapter 1: Introduction, Problem Statement and Literature Review

This chapter provides a comprehensive overview of the research landscape. It begins with the background and motivation for the study, highlighting the critical safety concerns associated with lithium-ion batteries and the necessity for accurate SOH and RUL estimation. It clearly states the primary goal of the thesis: to research and develop more accurate SOH and RUL estimation methods based on AI and provides necessary literature review. The chapter concludes by outlining the key contributions and the structure of the thesis.

Chapter 2: Overview of States Estimation Methods

This chapter lays the necessary theoretical foundation for the work. It provides detailed explanations of core concepts, including SOH, RUL, and PHM for LiBs. It delves into the electrochemical principles and physical

phenomena that cause battery degradation, such as SEI growth and lithium plating. Critically analyzing past and state-of-the-art methods for SOC, SOH and RUL prediction, comparing traditional approaches with modern ML and DL frameworks to establish the research gap this thesis aims to address.

Chapter 3: A CNN-BiGRU Temporal Attention Model for SOH and RUL Estimation

This chapter introduces the first proposed DL architecture: a hybrid model integrating CNN, BiGRU, and temporal attention. The chapter details the model's design and its application for estimating SOH and RUL using the public CALCE CS2-type battery dataset. It presents a rigorous comparative analysis, benchmarking the proposed CNN-BiGRU-Temporal Attention model against other established architectures like CNN, LSTM, CNN-BiLSTM, and BiLSTM-GRU. The performance is evaluated using metrics such as MAE, RMSE, and R^2, demonstrating the superiority of the proposed method.

Chapter 4: IPEformer: Inverted Patch Imbedding Transformer for SOH Estimation

This chapter presents the second and more advanced contribution of the thesis: the IPEformer model. This novel framework integrates a transformer-based DL architecture to enhance the accuracy and physical interpretability of SOH estimation. The chapter provides a complete description of the model and its training and testing on a diverse set of four public datasets (CALCE, NASA, MIT-Stanford, and XJTU) to demonstrate its robustness. The proposed model is then systematically compared with other models like CNN, LSTM, GRU and Attention, with evaluation based on MAE, RMSE, and R^2, confirming its enhanced performance.

Chapter 5: Experimental Battery Cycling and Validation on Proprietary Data

This chapter shifts focus to experimental data acquisition. It details the design and execution of a comprehensive battery cycling experiment conducted over six months on 9 cells (4 cylindrical and 5 pouch cells) until their end-of-life. The protocol for recording voltage, current, and temperature is specified. The proprietary dataset generated from this lengthy experiment is then used to validate the generalizability and real-world applicability of the proposed DL models from Chapters 3 and 4. The performance is rigorously evaluated using the standard metrics of RMSE, MAE, and R^2.

Chapter 6: Conclusion and Future Work

The final chapter summarizes the key findings and contributions of the thesis, synthesizing the results from both public dataset validation and proprietary experimental testing. It conclusively states the advancements made in SOH and RUL estimation accuracy through the proposed AI models. The chapter also discusses the limitations of the current work and provides a perspective on promising directions for future research, suggesting potential improvements to the models and new avenues for exploration in BMS.

2   Overview of States Estimation Methods

The hierarchical classification of Battery States estimation methods is shown in figure 2-1, the figure shows five principal methodological paradigms, each representing a distinct approach to addressing the complex challenge of battery state assessment. The foundation begins with Fundamental Modelling Paradigms (2.1), which establish the underlying physical and mathematical principles governing battery behavior, ranging from detailed electrochemical models to simplified ECM representations. Building upon these foundations, Model-Based Estimation Filters (2.2) leverage advanced state estimation techniques, including Kalman filter variants and observers, to recursively predict SOC, SOH and RUL by combining model predictions with real-time measurements. Complementing these PBMs, data-driven Estimation Methods (2.3) harness the power of ML and DL algorithms to extract complex degradation patterns directly from operational data without requiring explicit physical models. The emerging field of Hybrid Estimation Methods (2.4) represents a sophisticated integration of model-based and data-driven approaches, combining the interpretability of physical models with the adaptive capabilities of ML. Finally, Experimental and Measurement Techniques (2.5) encompass direct characterization methods that provide essential validation data and serve as benchmarks for data-driven approaches.
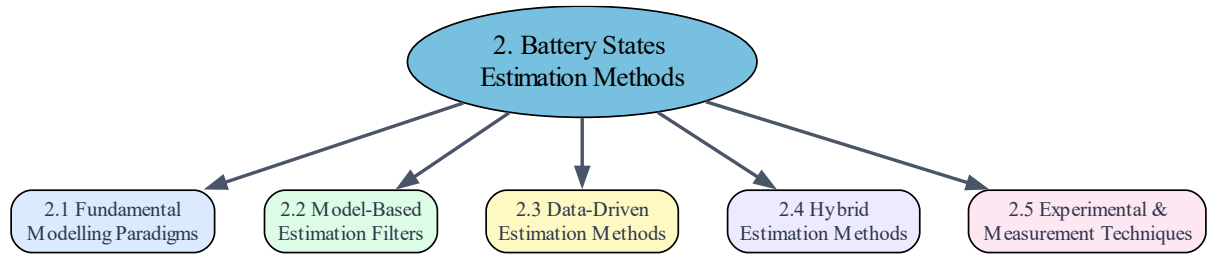
Figure 2-1: Taxonomy of Battery States Estimation Methodologies.

2.1 Fundamental modelling paradigms

The classification of Fundamental Modelling Paradigms for battery state estimation is given in figure 2-2, three distinct methodological approaches emerge, each offering unique trade-offs between physical interpretability and computational complexity. Electrochemical Models (White-Box) represent the most physically comprehensive approach, incorporating detailed electrochemical principles through formulations such as the pseudo-two-dimensional (P2D) Doyle-Fuller-Newman model, which captures intricate internal battery dynamics, along with simplified variants like the Single Particle Model (SPM) and its enhanced version with electrolyte dynamics (SPMe) that offer reduced computational burden while maintaining physical relevance. ECMs (Grey-Box) strike a balance between physical insight and practical implementation, utilizing electrical circuit analogs including the Thevenin model with resistor-capacitor networks, the Partnership for a New Generation of Vehicles (PNGV) model with added capacitance elements, and advanced fractional-order models that better represent the distributed electrochemical processes within battery systems. Data-Driven Models (Black-Box) complete the spectrum by employing purely empirical approaches that learn battery behavior patterns directly from operational data without explicit physical representations.

2.1.1 Electrochemical (White-Box) Modelling

  Electrochemical models capture the underlying physical and chemical phenomena of a battery.
While other models like ECMs and DDMs can only predict externally measurable cell quantities such as the terminal-voltage and surface-temperature in response to input-current. PBMs can predict more than these quantities, they can predict cell's internal electrochemical variables such as electrical potentials, lithium

concentrations, lithium fluxes, and temperatures. PBMs starting from molecular scale PDEs and particle scale PDEs are not possible to simulate in current desktop computers. However, DFN is a better suited to simulate although it is still not small enough to incorporate in a BMS. Using discrete-time realization algorithm (DRA), the complex DFN can be approximated to a low-order discrete-time state space model for lower computational complexity. The fundamental equation used in the DFN PBMs are given below:
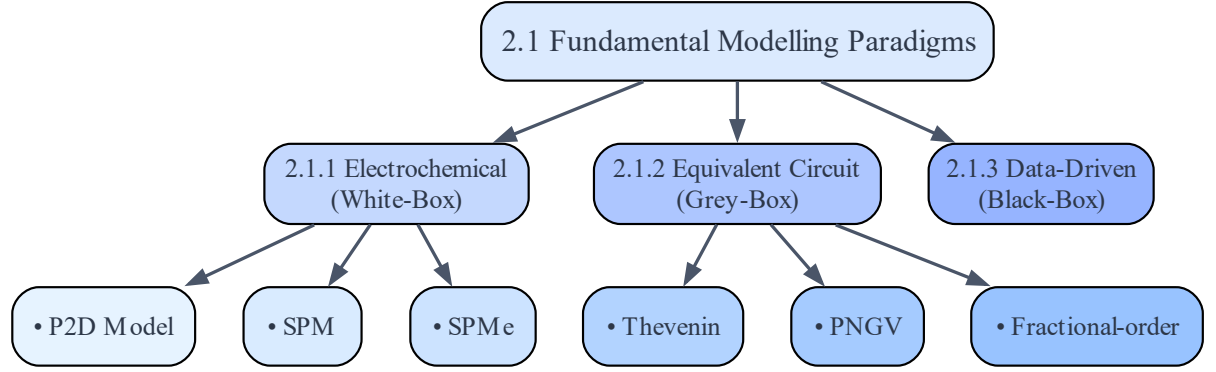
Figure 2-2: Hierarchical Classification of Fundamental Battery Models.

Charge conservation in solid

The charge conservation in the solid phase of the lithium-ion battery electrodes (both negative and positive) is governed by Ohm's law coupled with the volumetric current transfer rate at the electrode/electrolyte interface. The partial differential equation (PDE)

$$\frac{\partial}{\partial x}\left(\sigma_{eff}^r \frac{\partial \Phi_s^r}{\partial x}\right) = a_s^r F j^r, \tag{2-1}$$

states that the divergence of the effective ohmic current in the solid phase is balanced by the local Butler–Volmer reaction current, where σ_{eff}^r is the effective electronic conductivity of the electrode (accounting for the Bruggeman correction and active material volume fraction), Φ_s^r is the electric potential in the solid electrode phase, a_s^r is the specific interfacial surface area of the electrode particles (typically $a_s = 3\epsilon_s/R_s$ for spherical particles), F is Faraday's constant ($96485 Cmol^{-1}$), and j^r is the volumetric lithium transfer (reaction) current density (positive during discharge for the positive electrode and negative for the negative electrode).

Boundary conditions reflect the applied cell current and electrical insulation at the current-collector/electrode interfaces. At the current-collector contacts ($x = 0$ for the negative electrode and $x = L^{\text{tot}}$ for the positive electrode), the effective ohmic flux equals the applied current density:

$$\sigma_{\text{eff}}^n \frac{\partial \Phi_s^n}{\partial x}\bigg|_{x=0} = \sigma_{\text{eff}}^p \frac{\partial \Phi_s^p}{\partial x}\bigg|_{x=L^{\text{tot}}} = -\frac{i_{\text{app}}}{A}, \tag{2-2}$$

where i_{app} is the total electrical current measured at the cell terminals (positive during discharge) and A is the geometric surface area of the electrode plates. At the interfaces between electrode and separator ($x = L^n$ for the negative electrode and $x = L^n + L^s$ for the positive electrode), no electronic current crosses the separator, yielding a zero-flux (Neumann) condition:

$$\frac{\partial \Phi_s^n}{\partial x}\bigg|_{x=L^n} = \frac{\partial \Phi_s^p}{\partial x}\bigg|_{x=L^n+L^s} = 0, \tag{2-3}$$

The total cell thickness is defined as $L^{\text{tot}} = L^n + L^s + L^p$, where L^n, L^s, and L^p are the thicknesses of the negative electrode, separator, and positive electrode, respectively. Initial conditions are set at $t = 0$. The potential of the negative electrode is arbitrarily taken as the reference ($\Phi_{s,0}^n = 0$), while the initial potential of the positive electrode is chosen such that the cell open-circuit voltage at the beginning of the simulation is

recovered

$$\Phi_{s,0}^n = 0, \quad \Phi_{s,0}^p = u_{ocp}^p(\Theta_{s,0}^p) - u_{ocp}^n(\Theta_{s,0}^n). \tag{2-4}$$

where $\Theta_s^r = c_s^r / c_{s,max}^r$ is the local stoichiometric number (SOC) of the electrode ($0 \le \Theta_s^r \ge 1$), c_s^r is the lithium concentration in the solid particles, $c_{s,max}^r$ is the maximum stoichiometric lithium concentration, $\Theta_{s,0}^r = c_{s,0}^r / c_{s,max}^r$ is the initial equilibrium stoichiometry (uniform in each electrode), and $u_{ocp}^r(\Theta_s^r)$ is the open-circuit potential (OCP or equilibrium potential) of the electrode material expressed as a function of its local stoichiometry.

This equation applies only to the negative and positive electrode of the cell. It is a linear diffusion equation describing electron movement, with a forcing term that models flux of electrons.

Mass conservation in solid

The conservation of lithium mass within the active material particles of both the negative and positive electrodes is described by solid-phase diffusion, assuming spherical particles and concentration-independent diffusivity. The governing PDE is Fick's second law in radial coordinates:

$$\frac{\partial c_s^r}{\partial t} = \frac{1}{r^2}\frac{\partial}{\partial r}\left(D_s^r r^2 \frac{\partial c_s^r}{\partial r}\right), \tag{2-5}$$

where $c_s^r(r,t)$ is the lithium concentration in the solid particle of electrode r ($r = n$ for negative, $r = p$ for positive), D_s^r is the (constant) solid-phase diffusion coefficient of the electrode, and r is the radial coordinate inside a particle ($0 \le r \le R_s$).

At the particle surface ($r = R_s$), the diffusive flux is driven by the interfacial reaction current according to

$$D_s^r \frac{\partial c_s^r}{\partial r}\bigg|_{r=R_s} = j^r \tag{2-6}$$

where j^r (mol m^{-1} s^{-1}) is the molar lithium flux leaving the electrolyte and inserting into the solid (positive during charge for the positive electrode). At the particle center ($r = 0$), symmetry imposes zero flux:

$$\frac{\partial c_s^r}{\partial r}\bigg|_{r=0} = 0 \tag{2-7}$$

The initial lithium concentration in each electrode particle is assumed uniform and is set consistently with the desired initial cell SOC z_0 ($0 \le z_0 \le 1$):

$$c_{s,0}^r = c_{s,max}^r\left(\theta_0^r + z_0(\theta_{100}^r - \theta_0^r)\right). \tag{2-8}$$

where $c_{s,max}^r$ the maximum (theoretical) lithium concentration in the electrode material, θ_0^r is the normalized stoichiometry ($\theta^r = c_s^r / c_{s,max}^r$ of electrode r when the full cell is at 0% SOC, and θ_{100}^r is the corresponding stoichiometry when the full cell is at 100% SOC. This linear mapping ensures that $z_0 = 0$ recovers the fully discharged state and $z_0 = 1$ recovers the fully charged state for the entire cell. The fick's second law equations (often called the "single-particle diffusion" or "pseudo-2D" diffusion when coupled with the porous-electrode equations) are solved independently for every computational node along the through-plane direction in both electrodes, with the local surface flux j^r provided by the electrochemical kinetics (Butler–Volmer equation).

Charge conservation in electrolyte

Charge conservation in the electrolyte phase is governed by the concentrated solution theory for a binary electrolyte (typically LiPF$_6$ in organic solvent). The PDE states that the divergence of the effective ionic current is equal to the volumetric current transferred to the solid phase:

$$\frac{\partial}{\partial x}\left[\kappa_{eff}^r\left(\frac{\partial \Phi_e^r}{\partial x} + \frac{2RT(t_+^0 - 1)}{F}\left(1 + \frac{\partial \ln f_\pm}{\partial \ln c_e^r}\right)\frac{\partial \ln c_e}{\partial x}\right)\right] + a_s^r F j^r = 0, \tag{2-9}$$

where κ_{eff}^r is the effective ionic conductivity of the electrolyte (Bruggeman-corrected and usually concentration-dependent), Φ_e^r is the electrolyte potential, R is the universal gas constant, T is temperature, t_+^0 is the

transference number of the Li$^+$ cation with respect to the solvent velocity (typically ~ 0.38–0.4 for common electrolytes), , $f_\pm$ is the mean molar activity coefficient of the electrolyte (often assumed constant or fitted), c_e is the local electrolyte lithium-ion concentration, and the term in parentheses represents the thermodynamic driving force that includes both ohmic migration and a diffusional contribution arising from concentration gradients. Boundary conditions reflect the fact that no ionic current can flow through the current collectors. Zero total ionic flux is imposed at the left boundary ($x = 0$):

$$-\kappa_{\text{eff}}^r \left[\frac{\partial \Phi_e^r}{\partial x} + \frac{2RT(t_+^0 - 1)}{F} \left(1 + \frac{\partial \ln f_\pm}{\partial \ln c_e} \right) \frac{\partial \ln c_e^r}{\partial x} \right]\bigg|_{x=0} = 0, \tag{2-10}$$

while at the right boundary ($x = L^{\text{tot}}$), the ionic flux balances the applied cell current:

$$-\kappa_{\text{eff}}^r \left[\frac{\partial \Phi_e^r}{\partial x} + \frac{2RT(t_+^0 - 1)}{F} \left(1 + \frac{\partial \ln f_\pm}{\partial \ln c_e} \right) \frac{\partial \ln c_e^r}{\partial x} \right]\bigg|_{x=L^{tot}} = \frac{i_{\text{app}}}{A}. \tag{2-11}$$

Initially ($t = 0$), the electrolyte is at uniform concentration and at equilibrium, so the electrolyte potential is constant throughout the cell and set to cancel the open-circuit potential of the negative electrode (which was previously set to zero reference):

$$\Phi_{e,0}^r = -u_{\text{ocp}}^n(\Theta_{s,0}^n). \tag{2-12}$$

Mass conservation in electrolyte

The conservation of lithium ions in the electrolyte phase accounts for diffusion, migration (via the transference number), and the consumption/production of ions due to intercalation reactions at the electrode/electrolyte interfaces. The governing partial differential equation is

$$\frac{\partial \varepsilon_e^r c_e^r}{\partial t} = \frac{\partial}{\partial x}\left(D_{e,\text{eff}}^r \frac{\partial c_e^r}{\partial x} \right) + a_s^r(1 - t_+^0)j^r, \tag{2-13}$$

here $c_e^r(x,t)$ is the local lithium-ion concentration in the electrolyte within region r (negative electrode, separator, or positive electrode), ε_e^r is the local electrolyte volume fraction (porosity), $D_{e,\text{eff}}^r = D_e(c_e)\varepsilon_e^{\text{brugg}}$ is the effective diffusivity (often concentration-dependent and corrected by the Bruggeman relation), and the source term $a_s^r(1 - t_+^0)j^r$ represents the rate at which lithium ions are inserted into (or removed from) the electrolyte due to the electrochemical reaction (the factor $(1 - t_+^0)$ arises because only the fraction of current not carried by migration of Li$^+$ must be balanced by diffusion; this term is zero in the separator where $a_s^s = 0$).

No lithium flux can cross the current collectors, so zero diffusive flux (Neumann) boundary conditions are applied at the outer boundaries:

$$\frac{\partial c_e^n}{\partial x}\bigg|_{x=0} = \frac{\partial c_e^p}{\partial x}\bigg|_{x=L^{\text{tot}}} = 0, \tag{2-14}$$

At the two electrode/separator interfaces, both the diffusive flux and the concentration itself must be continuous:

$$D_{e,\text{eff}}^n \frac{\partial c_e^n}{\partial x}\bigg|_{x=(L^n)^-} = D_{e,\text{eff}}^s \frac{\partial c_e^s}{\partial x}\bigg|_{x=(L^n)^+}, \quad D_{e,\text{eff}}^s \frac{\partial c_e^s}{\partial x}\bigg|_{x=(L^n+L^s)^-} = D_{e,\text{eff}}^p \frac{\partial c_e^p}{\partial x}\bigg|_{x=(L^n+L^s)^+}, \tag{2-15}$$

$$c_e^n\big|_{x=(L^n)^-} = c_e^s\big|_{x=(L^n)^+}, \qquad c_e^s\big|_{x=(L^n+L^s)^-} = c_e^p\big|_{x=(L^n+L^s)^+}, \tag{2-16}$$

Initially, the electrolyte concentration is uniform throughout the cell:

$$c_e(x, 0) = c_{e,0}. \tag{2-17}$$

This completes the core set of governing equations for the standard DFN or P2D model of a lithium-ion battery, describing coupled charge and mass transport in both solid and electrolyte phases.

Kinetics (Butler-Voltage Equation)

The electrochemical kinetics of lithium insertion/de-insertion at the active material particle surface is modeled using the Butler-Volmer equation, which relates j^r to the surface overpotential η^r:

$$j^r = j_0^r \left[exp\left(\frac{(1-\alpha^r)F\eta^r}{RT}\right) - exp\left(\frac{-\alpha^r F\eta^r}{RT}\right) \right], \tag{2-18}$$

where α^r is the anodic charge-transfer coefficient (typically ≈ 0.5 if symmetric, otherwise fitted separately for each electrode). The concentration-dependent exchange current density j_0^r is given by the widely used form

$$j_0^r = k_{\text{norm},0}^r \left(\frac{c_e^r}{c_{e,0}^r}\right)^{1-\alpha^r} \left(1 - \frac{c_{s,e}^r}{c_{s,max}^r}\right)^{1-\alpha^r} \left(\frac{c_{s,e}^r}{c_{s,max}^r}\right)^{\alpha^r}, \tag{2-19}$$

with $k_{\text{norm},0}^r$ being the reaction-rate constant (in A m^{-2} (mol m^{-3})$^{-1.5}$, often separately parameterized for negative and positive electrodes), c_e^r the local electrolyte concentration, $c_{\{s,e\}}^r$ the surface concentration of lithium in the solid particle, and $c_{s,max}^r$ the maximum stoichiometric concentration. The local surface overpotential η^r is defined as the deviation from equilibrium, including an optional ohmic drop due to a surface film (SEI or CEI):

$$\eta^r = \Phi_s^r - \Phi_e^r - u_{ocp}^r \left(\frac{c_{s,e}^r}{c_{s,max}^r}\right) - FR_f^r j^r, \tag{2-20}$$

where Φ_s^r and Φ_e^r are the solid and electrolyte phase potentials, respectively, $u_{ocp}^r(\cdot)$ is the open-circuit potential (equilibrium potential) of electrode r as a function of surface stoichiometry, and R_f^r (Ω m^2) is the specific film resistance on the particle surface (often set to zero for the positive electrode and a small positive value or time-dependent for the negative electrode to represent SEI growth). When $R_f^r = 0$, the equation reduces to the standard Butler-Volmer form without film overpotential. This kinetic expression closes the coupling between solid-phase diffusion, electrolyte transport, and charge conservation in the full DFN model.

2.1.2 Equivalent circuit (Grey-Box) Modelling

ECMs represent the dynamic electrical behavior of a lithium-ion battery using a combination of voltage sources, resistors, and capacitors. They are "grey-box" because the open-circuit voltage (OCV) is derived from physical measurements, while the remaining parameters (resistances and capacitances) are empirically identified from experiments such as pulse tests or EIS. ECMs are computationally light and widely used in BMS, state estimation (SOC/SOH via Kalman filters), and real-time simulation.

General Structure and Governing Equations

The general n-RC ECM consists of an ideal voltage source $U_{ocv}(z)$ that depends non-linearly on the SOC z, a series (ohmic) resistance R_0, and n parallel RC branches capturing polarisation effects at different time scales. The terminal voltage $V(t)$ is

$$V(t) = U_{ocv}(z(t)) + I(t)R_0(z,T) + \sum_{k=1}^{n} V_k(t) \tag{2-21}$$

where $I(t)$ is the applied current (positive for discharge), and $V\_k(t)$ is the voltage across the k-th RC pair. The dynamics of each RC branch are

$$\dot{V}_k(t) = -\frac{V_k(t)}{R_k(z,T)C_k(z,T)} + I(t), \quad k = 1,...,n \tag{2-22}$$

or equivalently using time constant $\tau_k = R_k C_k$, The SOC evolution follows Coulomb counting:

$$\dot{z}(t) = -\frac{\eta I(t)}{Q_{\text{nom}}}, \tag{2-23}$$

where Q_{nom} is the nominal capacity (Ah) and $\eta \approx 1$ is the Coulombic efficiency. All parameters R_0, R_k, C_k (or τ_k) are typically stored as lookup tables or polynomials of SOC z and temperature T.

Common ECM Variants

Rint Model (0-RC): Simplest, only ohmic resistance.

$$V(t) = U_{ocv}(z) + IR_0. \tag{2-24}$$

Suitable only for very rough approximations.

1-RC Model (Thevenin Model): Captures fast charge-transfer dynamics (time constant ~10-30 s)

2-RC Model: Most popular compromise between accuracy and complexity. The first RC pair models fast processes (charge transfer, SEI), the second slower diffusion-like phenomena (100-500 s). n-RC Model ($n \geq 3$): Higher-order models for improved accuracy at very low frequencies or strong diffusion tails Randle's Model with Warburg Element: Used when EIS data show clear 45° diffusion lines. Replaces the slowest RC pair with a Warburg impedance $Z_W = \sigma_W/\sqrt{j\omega}$ (or its finite-space approximation)

2.2 Model based estimation filters

Based on the classification of model-based estimation filters for battery SOH assessment, three principal algorithmic families emerge as the cornerstone of modern state estimation techniques.
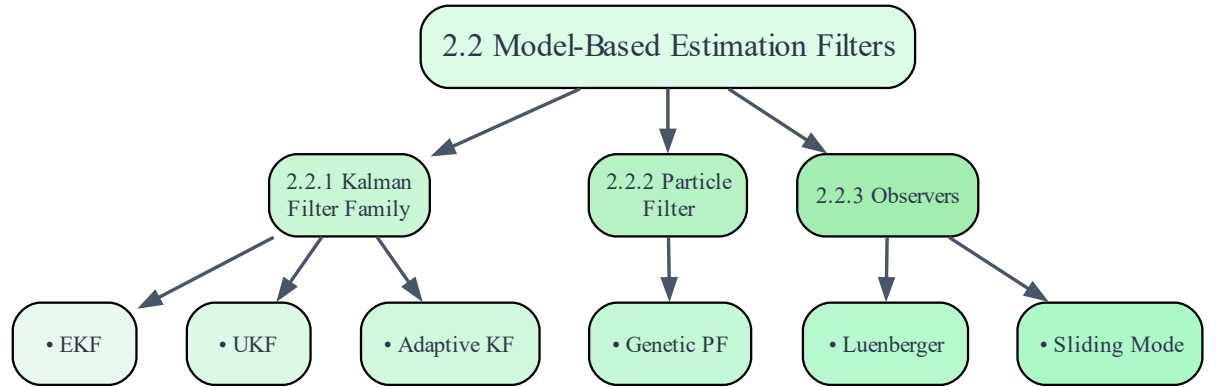
Figure 2-3: Model-Based Filtering Approaches for Battery States Estimation.

2.2.1 Kalman Filter (KF) and Its Main Variants for Battery State Estimation

The KF is the optimal linear estimator for the state of a linear dynamic system corrupted by Gaussian noise. It operates in two steps: prediction (time update) and correction (measurement update). For a discrete-time linear system:

$$x_k = Ax_{k-1} + Bu_{k-1} + w_{k-1}, \tag{2-25}$$

$$z_k = Hx_k + v_k \tag{2-26}$$

where $w \sim N(0, Q)$ and $v \sim N(0, R)$ are process and measurement noise, the classic Kalman filter prediction equations are as follows:

$$\hat{x}_{k|k-1} = A\,\hat{x}_{k-1|k-1} + B\,u_{k-1} \tag{2-27}$$

$$P_{k|k-1} = AP_{k-1|k-1}A^T + Q, \tag{2-28}$$

And the correction or measurement update is given by:

$$K_k = P_{k|k-1}H^T\left(HP_{k|k-1}H^T + R\right)^{-1} \tag{2-29}$$

$$\hat{x}_{k|k} = \hat{x}_{k|k-1} + K_k\left(z_k - H\hat{x}_{k|k-1}\right), \tag{2-30}$$

$$P_{k|k} = (I - K_kH)P_{k|k-1}, \tag{2-31}$$

where $\hat{x}_{k|k-1}$ is the predicted state, $P_{k|k-1}$ the predicted covariance, K_k the Kalman gain, Q the process noise covariance, and R the measurement noise covariance.

In battery applications (typically ECM-based), the state vector x usually contains SOC z and the voltages across the RC pairs ($V1, V2, ...$).

$$x_k = [z_k \quad V_{1,k} \quad V_{2,k} \quad \cdots]^T \tag{2-32}$$

The KF provides unbiased minimum-variance estimates when the model is linear and noise is Gaussian. The Extended Kalman Filter (EKF) extends the KF to nonlinear systems by performing local linearization around the

current estimate using the Jacobian matrices. The system becomes

$$x_k = f(x_{k-1}, u_{k-1}) + w_{k-1}, \tag{2-33}$$

$$z_k = h(x_k) + v_k \tag{2-34}$$

Prediction remains the same as KF but with

$$A_k = \left.\frac{\partial f}{\partial x}\right|_{\hat{x}_{k-1|k-1}}, \qquad H_k = \left.\frac{\partial h}{\partial x}\right|_{\hat{x}_{k|k-1}} \tag{2-35}$$

evaluated at the current estimate. The correction step uses the linearized matrices exactly as in the classic KF. EKF is the most widely used algorithm for joint SOC and SOH estimation on ECMs because the OCV-SOC relationship is strongly nonlinear while the rest of the model is nearly linear. The Unscented Kalman Filter (UKF) avoids linearization errors of the EKF by using the unscented transformation. It propagates a set of carefully chosen sigma points through the true nonlinear functions $f(\cdot)$ and $h(\cdot)$, then recovers mean and covariance from the transformed points. UKF typically achieves higher accuracy than EKF (especially around flat OCV regions of LFP cells) with similar computational cost and no need to compute Jacobians.

The Sigma-Point Kalman Filter (SPKF) is a general class that includes UKF and other variants (central difference KF, etc.). It relies entirely on deterministic sampling of the state distribution.

The Adaptive Kalman Filter (AKF) and Adaptive Extended Kalman Filter (AEKF) estimate the process noise covariance Q and/or measurement noise covariance R online (usually via covariance matching or multiple-model approaches) to cope with changing battery dynamics, temperature, and ageing. The Dual Kalman Filter (DKF) and Dual Extended Kalman Filter (DEKF) run two filters simultaneously: one for the state (SOC, RC voltages) and one for slowly varying parameters (capacity Q_{nom} and resistances). This enables simultaneous SOC and SOH estimation. The Square-Root Kalman Filters (SR-EKF, SR-UKF) propagate the square root of the covariance matrix to improve numerical stability and guarantee positive semi-definiteness of P, which is critical in embedded BMS implementations. In practice today, EKF and DEKF remain the industry standard in automotive and consumer BMS because of their low memory footprint and maturity, while UKF and AEKF/DEKF are increasingly adopted in research and high-performance applications where higher accuracy justifies the modest extra computation.

2.2.2 Particle Filter (PF)

PF is a sequential Monte Carlo method that represents the posterior probability density of the state (SOC, SOH, RC voltages) using a set of weighted particles $x_k^{(i)}, w_k^{(i)} i = 1^N$. The algorithm performs prediction by propagating each particle through the nonlinear ECM dynamics $x_k^{(i)} \sim p(x_k | xk - 1^{(i)}, u_k)$, followed by weight update $w_k^{(i)} \propto w_{k-1}^{(i)} p\left(V_k | x_k^{(i)}\right)$ using the likelihood of the measured voltage, and resampling when degeneracy occurs. The final estimate is the weighted mean

$$\hat{x}_{k|k} = \sum_{i=1}^{N} w_k^{(i)} x_k^{(i)}. \tag{2-36}$$

PF handles strong nonlinearities (e.g., flat OCV plateaus in LFP cells) and non-Gaussian noise far better than EKF/UKF, achieving lower SOC error in challenging conditions, but requires 500-5000 particles and is therefore mostly used offline or in high-performance BMS.

Genetic Particle Filter (GPF)

GPF improves the standard PF by incorporating genetic algorithm operators (crossover and mutation) during the resampling step to increase particle diversity and prevent particle impoverishment. After computing weights, selected high-weight particles undergo crossover and mutation before replacement, significantly reducing

estimation variance in long-horizon SOH tracking and multimodal distributions caused by ageing uncertainties.

Luenberger Observer (LBO)

LBO is a deterministic full-order observer adapted to nonlinear ECMs. For a system $\dot{x} = f(x, u), V = h(x)$, the observer dynamics are

$$\dot{\hat{x}} = f(\hat{x}, u) + L(V - \hat{V}),\qquad(2\text{-}37)$$

where L is the observer gain chosen such that the error system $\dot{e} = (A - LC)e +$ nonlinear terms is globally asymptotically stable (often proved via Lyapunov functions). Simple proportional gain or high-gain designs work well for SOC estimation with small steady-state error.

Sliding Mode Observer (SMO)

SMO enhances robustness by introducing a discontinuous switching term that forces the voltage estimation error onto a sliding surface in finite time. The typical structure for battery ECM is

$$\dot{\hat{z}} = -\frac{\eta I}{Q} + k_1 \text{sign}(V - \hat{V}),\qquad(2\text{-}38)$$

$$\dot{\widehat{V_{RC}}} = -\frac{\widehat{V_{RC}}}{\tau} + \frac{I}{C} + k_2 \text{sign}(V - \hat{V}),\qquad(2\text{-}39)$$

$$\hat{V} = U_{\text{ocv}}(\hat{z}) + IR_0 + (\hat{V})_{RC},\qquad(2\text{-}40)$$

where the sign function is often replaced by saturation or super-twisting algorithms to reduce chattering. SMO is extremely popular in automotive and aerospace BMS because it provides finite-time convergence and inherent robustness against parameter variation, temperature changes, and sensor noise, often outperforming EKF-based methods in real-world driving cycles while requiring minimal tuning.

2.3 Data-driven estimation methods

Based on the classification of data-driven and hybrid approaches for battery SOH estimation, two transformative paradigms have emerged that leverage computational intelligence to overcome limitations of traditional model-based methods. Data-Driven Estimation Methods (2.3) encompass ML techniques that learn complex battery degradation patterns directly from operational data, divided into Classical ML approaches including Support Vector Regression (SVR) for high-dimensional pattern recognition, Gaussian Process Regression (GPR) for probabilistic predictions with uncertainty quantification, and Random Forest ensemble methods for robust feature-based forecasting; and DL architectures that capture temporal dependencies through LSTM/GRU networks, extract spatial features via CNN implementations, and employ advanced Transformer models for capturing long-range dependencies in battery aging data. Complementing these purely data-driven approaches, Hybrid Estimation Methods (2.4) represent the cutting edge of SOH estimation by synergistically combining physical knowledge with data-driven adaptability through Model-Data Fusion frameworks that integrate physics-based constraints with neural networks, Adaptive Filters with ECMs that continuously update model parameters using real-time data, Ensemble Frameworks that aggregate predictions from multiple diverse models, and ICA/DVA with ML approaches that leverage features from incremental capacity and differential voltage analysis as inputs to ML algorithms.

These methodologies collectively address the fundamental challenge of battery SOH estimation by either learning complex nonlinear relationships directly from data or creating powerful synergies between physical understanding and data-driven adaptability, enabling more accurate and robust health monitoring without requiring complete first-principles knowledge of underlying degradation mechanisms.
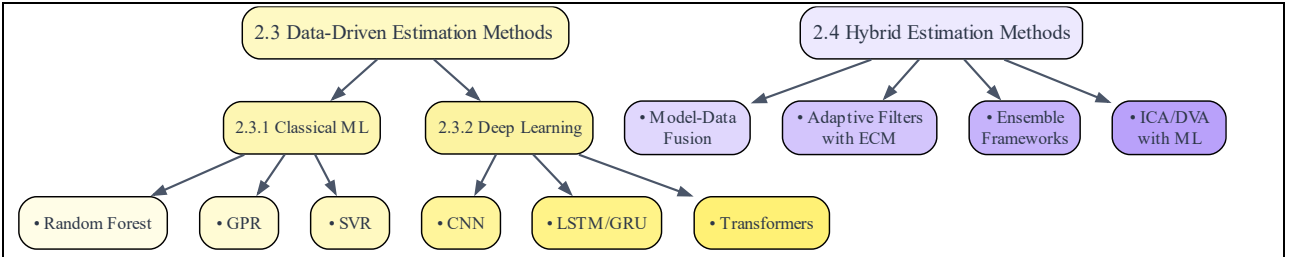
Figure 2-4: ML and Hybrid Battery States Estimation Frameworks.

2.3.1 Classical ML based methods

Classical machine learning approaches treat SOH estimation as a regression (or classification) problem by extracting health indicators (features) from measured voltage, current, temperature, and impedance data during partial or full cycles, then training models to map these features to capacity or internal resistance.

Support Vector Machine Regression (SVR)

SVR seeks a function $f(x) = w^T \phi(x) + b$ that deviates by at most ϵ from the true capacity Q for all training points while keeping the norm $||w||$ as small as possible. Introducing slack variables ξ_i, ξ_i^*, the optimization problem becomes

$$\min_{w,b,\xi,\xi^*} \frac{1}{2} ||w||^2 + C \sum_{i=1}^{m} (\xi_i + \xi_i^*) \tag{2-41}$$

subject to

$$Q_i - (w^T \phi(x_i) + b) \leq \varepsilon + \xi_i, \quad (w^T \phi(x_i) + b) - Q_i \leq \varepsilon + \xi_i^*, \quad \xi_i, \xi_i^* \geq 0. \tag{2-42}$$

Using the kernel (usually RBF kernel $k(x_i, x_j) = \exp(-\gamma|x_i - x_j|^2)$, SVR is applied for SOH prediction from incremental capacity and differential voltage features.

Random Forest Regression (RFR)

RFR is an ensemble of decision trees trained on bootstrap samples of the data, with random feature selection at each split. The prediction is the average over all trees:

$$\hat{y}(x) = \frac{1}{T} \sum_{t=1}^{T} h_t(x), \tag{2-43}$$

where $h_t(x)$ is the output of the t-th tree and T is usually hundreds. RFR is resistant to overfitting, provides built-in feature importance scores, and estimates SOH without requiring extensive hyper-parameter tuning.

Gaussian Process Regression (GPR)

GPR is a non-parametric Bayesian method that places a Gaussian process prior over functions: $f(x) \sim GP(m(x), k(x, x'))$. For zero mean and a chosen kernel (commonly squared-exponential), the predictive distribution at a new input x_* is

$$\mu(x_*) = k_*^T (K + \sigma_n^2 I)^{-1} y, \tag{2-44}$$
$$\sigma^2(x_*) = k(x_*, x_*) - k_*^T (K + \sigma_n^2 I)^{-1} k_*, \tag{2-45}$$

where K is the kernel matrix of training inputs and k_* the kernel vector between x_* and training points. GPR naturally quantifies prediction uncertainty which is critical for safety-related battery diagnostics and performs well when only a few dozen ageing cycles are available for training, despite its $O(N^3)$ scaling.

2.3.2 DL based methods

DL approaches have gained popularity for SOH estimation by directly processing raw or minimally pre-processed time-series data (voltage, current, temperature sequences) or spectrogram-like inputs (e.g., EIS impedance images), eliminating much of the manual feature engineering required in classical methods.

Convolutional Neural Networks (CNNs)

CNNs excel at extracting local patterns from charge/discharge voltage curves or incremental capacity (IC/DV) spectra treated as 1D signals. A typical 1D CNN layer performs convolution as

$$y[j] = \sum_{m=0}^{M-1} x[j+m] \cdot w[m] + b,$$

(2-46)

followed by ReLU activation and pooling. Stacked convolutional blocks automatically learn health-related features such as peak shifts and area degradation in IC curves, while fully connected layers at the end regress SOH or remaining useful life (RUL).

Long Short-Term Memory (LSTM)

LSTM networks are recurrent architectures designed to model long-term dependencies in sequential battery cycling data. Each LSTM cell updates its hidden state h_t and cell state c_t using three gates:

$$i_t = \sigma(W_i x_t + U_i h_{t-1} + b_i), \quad f_t = \sigma\big(W_f x_t + U_f h_{t-1} + b_f\big),$$

(2-47)

$$o_t = \sigma(W_o x_t + U_o h_{t-1} + b_o), \quad \widetilde{c}_t = \tanh(W_c x_t + U_c h_{t-1} + b_c),$$

(2-48)

$$c_t = f_t \odot c_{t-1} + i_t \odot \widetilde{c}_t, \quad h_t = o_t \odot \tanh(c_t),$$

(2-49)

where σ is the sigmoid function and $\odot$ denotes element-wise multiplication. LSTMs effectively capture gradual capacity fade trends over hundreds of cycles and are widely applied for RUL prediction from raw voltage-current-time series.

Gated Recurrent Units (GRU)

GRU are a simplified yet equally powerful variant of LSTM with fewer parameters. A GRU cell combines forget and input gates into an update gate z_t and introduces a reset gate r_t:

$$z_t = \sigma(W_z x_t + U_z h_{t-1}), \quad r_t = \sigma(W_r x_t + U_r h_{t-1}),$$

(2-50)

$$\widetilde{h}_t = \tanh\big(W_h x_t + U_h(r_t \odot h_{t-1})\big), \quad h_t = (1 - z_t) \odot h_{t-1} + z_t \odot \widetilde{h}_t.$$

(2-51)

GRUs train faster than LSTMs while delivering comparable or slightly better performance on most battery ageing sequences, making them the preferred recurrent architecture in recent SOH and RUL studies.

Transformers

Transformers were originally developed for natural language processing but recently they have dominated battery prognostics through their self-attention mechanism that directly models relationships between any two points in a sequence regardless of distance. The scaled dot-product attention is computed as

$$\text{Attention}(Q, K, V) = \text{softmax}\left(\frac{QK^T}{\sqrt{d_k}}\right) V,$$

(2-52)

where Q, K, V are query, key, and value projections of the input sequence, and multi-head attention runs several attention functions in parallel. Combined with positional encoding and feed-forward layers, Transformers outperform LSTMs/GRUs on long cycling.

2.4 Hybrid Estimation methods

Hybrid models combine two or more methods to make the prediction more robust and accurate. It could be a PBM combined with AI or ECM with ML. Below is some of these combinations for hybrid models.

Model-Data Fusion (Hybrid) Methods

This type of hybrid methods combine battery model (typically equivalent circuit or reduced-order DFN) with data-driven correction to achieve high accuracy and extrapolative capability. A common formulation uses an ECM to predict voltage $\widehat{V_k} = U_{ocv}(z_k) + I_k R_0 + \sum V_{i,k}$, then treats model mismatch as a residual that a machine learning model (e.g., GPR, NN) learns:

$$SOH_k = f_{model}(z_k, \theta) + g_{ML}(\text{features}_k),$$

(2-53)

or more frequently in dual/joint estimation, parameters (capacity Q and resistance R₀) are updated online via Bayesian filtering while a neural network corrects systematic model errors. This yields lower error even when extrapolating to new chemistries or temperatures.

Adaptive Filters with ECM

It extends classical Kalman-based methods by simultaneously estimating both state (SOC, RC voltages) and slowly varying parameters $(Q_{\text{nom}}, R_0, R_1 \dots)$. The Dual Extended Kalman Filter (DEKF) runs two intertwined EKFs:

State filter: $\hat{x}_{k|k} = \hat{x}_{k|k-1} + K_k^x(V_k - \hat{V}_k)$

Parameter filter: $\hat{\theta}_{k|k} = \hat{\theta}_{k|k-1} + K_k^\theta(V_k - \hat{V}_k)$

where $\theta = [Q, R^0, R^1, C^1 \dots]$. Adaptive covariance tuning (AEKF) or multiple-model approaches further improve robustness, making these methods standard for online SOH tracking in production BMS.

Ensemble Frameworks combine multiple diverse models (e.g., SVR + GPR + LSTM + 2-RC PF) to reduce individual weaknesses. The final SOH prediction is typically a weighted average

$$\hat{y} = \sum_{m=1}^{M} w_m \hat{y}_m, w_m \propto \exp(-\lambda \text{RMSE}_m^{\text{val}}) \tag{2-54}$$

or Bayesian model averaging using posterior probabilities. Ensembles consistently achieve the lowest errors) on heterogeneous datasets and are the current state-of-the-art when computational budget allows offline or cloud-based estimation.

Incremental Capacity Analysis (ICA) and Differential Voltage Analysis (DVA) with ML

It remains highly effective hybrid feature-based approaches. ICA computes dQ/dV and DVA dV/dQ from low-rate charge/discharge curves, revealing characteristic peaks/valleys that shift and diminish with ageing. Features such as peak position, height, area, and spacing are extracted and fed to simple ML models (Random Forest, GPR, shallow NN):

$$\text{SOH} = f_{ML}\left(peak_1^{height}, peak_2^{position}, \Delta area, \dots\right) \tag{2-55}$$

This physics-informed feature + ML pipeline routinely delivers <1.5 % error using only one full reference cycle for training and is widely used in second-life screening and fast diagnostics.

2.5 Experimental and Measurement Techniques

Based on the classification of experimental and measurement techniques for battery SOH assessment, two complementary approaches provide essential physical validation and direct characterization capabilities that serve as critical benchmarks for data-driven and model-based methods: Direct Measurement and Advanced Techniques as shown in figure 2-5.
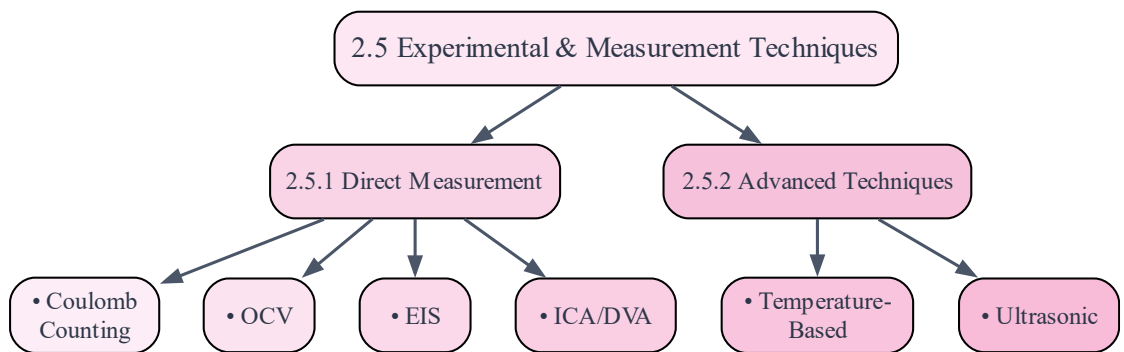
Figure 2-5: Experimental Characterization Techniques for Battery states estimation

2.5.1 Direct Measurement Techniques

These methods encompass established laboratory and operational methods including Coulomb Counting for tracking capacity fade through charge throughput accounting, Open-Circuit Voltage (OCV) Measurement that correlates voltage relaxation patterns with SOC and degradation, Electrochemical Impedance Spectroscopy (EIS) which characterizes internal resistance and charge transfer dynamics across frequency domains, and Incremental Capacity Analysis/Differential Voltage Analysis (ICA/DVA) that identifies phase transition features in voltage curves to quantify active material loss and degradation mechanisms.

Coulomb Counting (Ampere-Hour Integration)

It is the simplest and most widely used direct method for online SOC estimation in BMS integrating the measured current over time:

$$z(t) = z(t_0) - \frac{1}{Q_{nom}} \int_{t_0}^{t} \eta I(\tau) \, d\tau, \tag{2-56}$$

where $z(t_0)$ is the initial SOC (often from OCV), η the Coulombic efficiency ($\approx 0.99 - 1.0$), and Q_{nom} the nominal capacity. Although straightforward, it suffers from cumulative drift due to current-sensor bias and requires periodic recalibration (e.g., at full charge or via OCV).

Open-Circuit Voltage (OCV) Method

This method exploits the monotonic (or piecewise-monotonic) relationship between equilibrium voltage and SOC/SOH after sufficient relaxation (typically > 2–8 h):

$$z = f_{OCV}^{-1}(U_{ocv}), \quad SOH = \frac{Q_{current}}{Q_{rated}} \tag{2-57}$$

The OCV–SOC curve is obtained experimentally at very low C-rate (C/20–C/50) or via GITT (Galvanostatic Intermittent Titration Technique). It is highly accurate (± 1 % SOC) when relaxation is complete but impractical during operation; therefore, it is mainly used for initial SOC determination after long rest or for offline capacity testing.

Electrochemical Impedance Spectroscopy (EIS)

This experimental method applies a small AC signal (mV amplitude) over a wide frequency range (mHz to kHz) and measures the complex impedance response $Z(\omega)$. The Nyquist plot typically reveals ohmic resistance R_0 (high-frequency intercept), charge-transfer semicircle (mid-frequency), and diffusion tail (low-frequency). Ageing parameters are extracted by fitting to an equivalent circuit:

$$Z(\omega) = R_0 + \frac{R_{ct}}{1 + j\omega R_{ct} C_{dl}} + Z_W(\omega), \tag{2-58}$$

where Z_W is the Warburg element. Increase in R_0 and R_{ct} strongly correlates with SOH loss (SEI growth, contact degradation). EIS is the gold standard for non-destructive internal-state diagnosis but requires specialized equipment and is usually performed offline or at specific SOC points.

Capacity Analysis and Incremental Capacity/Differential Voltage Analysis (ICA/DVA)

These methods are low-rate diagnostic techniques that reveal degradation mechanisms. During constant-current charge/discharge at C/20–C/50, ICA computes

$$\frac{dQ}{dV} = \frac{I \cdot \Delta t}{\Delta V}, \tag{2-59}$$

and DVA computes

$$\frac{dV}{dQ} = \frac{\Delta V}{I \cdot \Delta t}. \tag{2-59}$$

Peaks in IC curves correspond to phase transitions in electrode materials; their height reduction and position

shift directly indicate loss of active material and lithium inventory. These curves serve as highly informative health features for both classical and deep-learning SOH models and are considered essential reference tests in battery research and second-life assessment.

2.5.2 Advanced Techniques

These methods employ sophisticated sensing methodologies such as Ultrasonic Inspection that probes internal structural changes through acoustic wave propagation analysis, and Temperature-Based Methods that monitor thermal signatures and entropy variations to detect internal short circuits and material degradation. These experimental techniques provide the fundamental ground truth data essential for validating model predictions and training ML algorithms, while also offering direct physical insights into degradation mechanisms that cannot be fully captured by computational approaches alone, thereby establishing the empirical foundation upon which all other SOH estimation methods ultimately depend for verification and refinement.

Temperature-Based Methods

This method uses the strong correlation between internal temperature distribution, heat generation rate, and degradation mechanisms (SEI growth, lithium plating, etc.). Surface temperature is measured with thermocouples or infrared cameras, while core temperature can be estimated using impedance-based electro-thermal models or embedded sensors. The heat generation rate is calculated from

$$q = I(V - U_{\text{ocv}}) - T\frac{dU_{\text{ocv}}}{dT}I, \tag{2-60}$$

where the first term represents Joule and overpotential heating, and the second the reversible entropic heat. Differential thermal voltammetry (DTV) plots dT/dV or dT/dt during low-rate cycling, revealing peaks corresponding to phase transitions that shift with ageing. Temperature rise during high-rate pulses or entropy coefficient $\frac{dU_{\text{ocv}}}{dT}$ variation serve as low-cost SOH indicators, achieving low accuracy without capacity tests.

Ultrasonic Techniques

These are emerging non-destructive methods that use high-frequency acoustic waves (0.1–10 MHz) transmitted through the battery to detect internal structural changes. A pulse-echo or through-transmission setup measures time-of-flight (ToF), signal amplitude, and frequency spectrum. The wave velocity c and attenuation coefficient α relate to S/OC and health via

$$c = \sqrt{\frac{E(1-\nu)}{\rho(1+\nu)(1-2\nu)}}, \tag{2-61}$$

where E, ν, and ρ are effective modulus, Poisson ratio, and density influenced by lithiation level and mechanical degradation (cracks, gas pockets, electrode delamination). Ageing causes increased attenuation and ToF shifts due to SEI thickening and particle fracture. Ultrasonic monitoring can detect lithium plating in real time (via strong reflection from dendritic layers) and estimate SOH with lower error in laboratory settings, offering a promising contactless, fast, and inline diagnostic tool for manufacturing and second-life screening.

External Magnetic Field detection

This emerging diagnostic technique leverages the magnetic field generated externally around a lithium-ion battery pack during operation to detect inconsistencies (e.g., capacity imbalance, uneven SOC/SOH, or faults) among parallel-connected cells without disassembly or invasive probes. When a pack (typically cells in parallel) carries current, each cell contributes to the total magnetic field according to Ampere's law (Biot-Savart principle): the magnetic field B at a point outside the pack is the superposition

$$B(r) = \frac{\mu_0}{4\pi}\sum_i I_i \int \frac{dl_i \times (r - r')}{|r - r'|^3}, \tag{2-62}$$

where I_i is the current in the i-th current path (cell or busbar), μ_0 the permeability of free space, and the integral is over the conductor paths.

In a healthy balanced pack, currents I_i are equal, producing a symmetric and predictable B-field pattern. Capacity/SOC inconsistency forces uneven current sharing (a weaker cell carries less current in parallel during charge/discharge), creating detectable asymmetries or anomalies in the external magnetic field map. By scanning the field above the pack using arrays of sensitive sensors (e.g., Hall probes, anisotropic magnetoresistive (AMR) sensors, or optically pumped magnetometers), a 2D/3D magnetic image is constructed and inverted to reconstruct local current imbalances with milliampere resolution.

3 CNN-BiGRU with Temporal Attention based PHM

SOH and RUL are critical indicators for prognostics, such as accessing performance, planning maintenance, and ensuring operational reliability. In this chapter we ar going to apply of deep neural network architecture through integration of CNN-BiGRU and temporal attention for estimating SOH and RUL. The proposed method CNN–BiGRU-Temporal Attention is rigorously compared with other established DL architectures such as CNN, LSTM, CNN-BiLSTM, and BiLSTM-GRU. And , the proposed method with other benchmark models, is evaluated using various metrics such as MAE, RMSE, and R^2, showing that the model has better results and contributes to developing reliable and safer BMS.

3.1 Dataset description

In this research, we use the CALCE CS2 battery dataset. Four CS2 prismatic cells went through the same charging and discharging profile. Constant current, constant voltage (CCCV) was employed for charging and discharging at various temperatures. Additional technical information is provided in Table 2.1.

TABLE 3-1 Characteristics comparison of different battery chemistries

Parameters	Values
Dataset	CALCE CS2
Cells	CS2_35, CS2_36, CS2_37, CS2_38
Chemistry	$LiCoO_2$ (LCO)
Dimensions	$5.4 \times 33.6 \times 50.6$ mm
Nominal Voltage	3.6 V
Energy Capacity	1.1 Ah
Charging Current	0.55 A
Discharging Current	1.1 A
Voltage Range	4.2 V to 2.7 V (discharge)

Over the lifetime of the battery, it undergoes charging and discharging cycles, which results in gradual degradation of its performance. This degradation in performance over time is called aging, which decreases the SOH of the battery. Capacity degradation of different cells can be seen in Fig. 1. We calculate SOH in its capacity form defined in equation (3-1). Similarly, the true and predicted RUL are shown in equation (3-2) and equation (3-3), respectively.
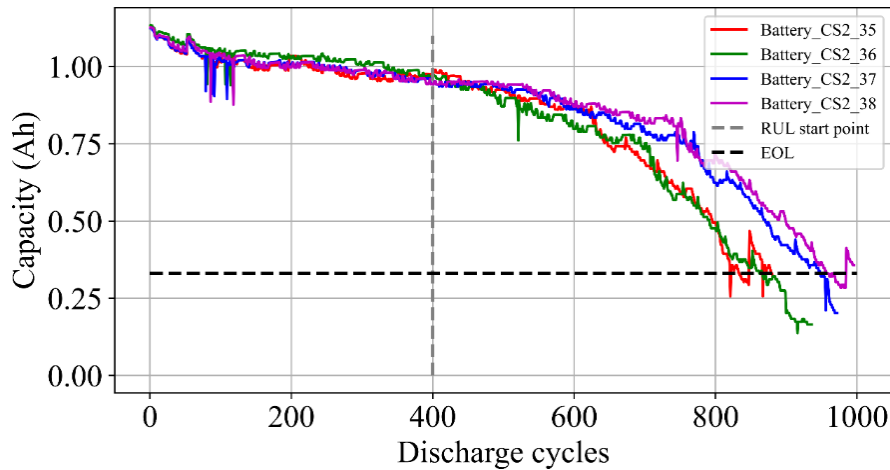
Figure 3-1: Capacity degradation of the CALCE dataset over discharge cycles. The 70 % capacity threshold line indicates the commonly accepted EOL criterion for LiBs

We calculate SOH in its capacity form defined in equation 2-1. Similarly, true and predicted RUL are shown in equation 3-2 and 3-3 respectively.

$$SOH = \frac{C_{current}}{C_{rated}} \times 100\% \tag{3-1}$$

Where, $C_{current}$ is the measured capacity of the battery and C_{rated} is the rated or initial capacity.

$$RUL_{true} = N_{EOL}^{true} - N_{current} \tag{3-2}$$

$$RUL_{pred} = N_{EOL}^{pred} - N_{current} \tag{3-3}$$

where N_{EOL}^{true} and N_{EOL}^{pred} are the true and predicted end-of-life cycles, respectively, and $N_{current}$ is the RUL monitoring cycle.

3.2 Evaluation metrics

To measure the accuracy of the model in SOH and RUL estimation, RMSE, MAE, R^2, and RUL absolute error (RUL_{error}) are used. The corresponding formula is as follows:

$$Root\ Mean\ Square\ Error (RMSE) = \sqrt{\frac{1}{n}\sum_{i=1}^{n}\left(SOH_{true,i} - SOH_{pred,i}\right)^2} \tag{3-4}$$

$$Mean\ Absolute\ Error (MAE) = \frac{1}{n}\sum_{i=1}^{n}\left|SOH_{true,i} - SOH_{pred,i}\right|, \tag{3-5}$$

$$Coefficient\ of\ determination\ R_{SOH}^2 = 1 - \frac{\sum_{i=1}^{n}\left(SOH_{true,i} - SOH_{pred,i}\right)^2}{\sum_{i=1}^{n}\left(SOH_{true,i} - SOH_{true}\right)^2}, \tag{3-6}$$

$$Remaining\ Useful\ Life\ (RUL)\ Error = \left|RUL_{pred} - RUL_{true}\right| (in\ cycles) \tag{3-7}$$

$SOH_{true,i}$ is the actual SOH value at index i, $SOH_{pred,i}$ is the predicted SOH value at index i, SOH_{true} is the mean of the actual SOH values, and n is the total number of data points. RUL_{error} is the absolute error between RUL_{true} and RUL_{pred}.

3.2 Methodology

This section presents the modeling, development, and working of our proposed method. Below is the detailed explanation.

3.2.1 CNN for short-term feature extraction

CNN in the proposed method serves as a local feature extractor that identifies spatially correlated temporal patterns in the battery dataset. By applying one-dimensional (1D) convolutions, CNN captures short-term degradation signatures and learns hierarchical representations where deeper layers encode complex degradation behaviors. The convolutional operation is expressed as:

$$h_i^{(k)} = f\left(W^{(k)} * x_{i:i+s-1} + b^{(k)}\right), \tag{3-8}$$

where $W^{(k)}$ and $b^{(k)}$ denote the kernel weights and bias of the k-th filter, s is the kernel size, and f is a nonlinear activation function. This process reduces noise, enhances generalization, and improves computational efficiency. The extracted feature maps are subsequently fed into the BiGRU.

3.2.2 BiGRU for long-term feature extraction

GRU networks are widely used for sequence modeling tasks and have shown strong performance in battery SOH estimation due to their ability to capture long-term dependencies from complex input patterns. In this

work, a BiGRU architecture is adopted (see Figure 3-2 and Figure 3-3) to further improve the learning of temporal correlations by processing data in both forward and backward directions.
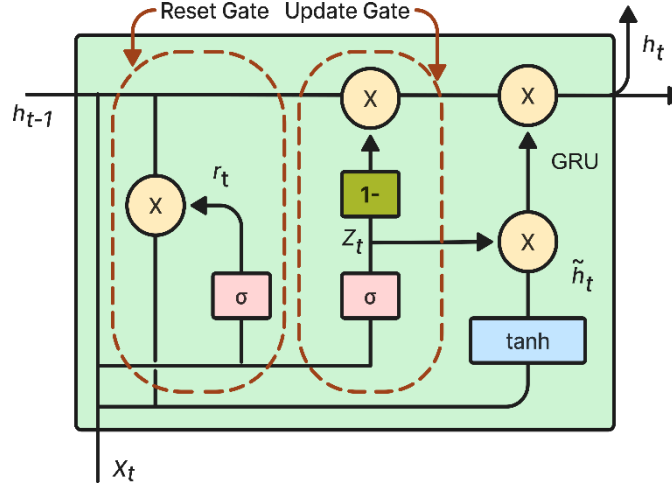
Figure 3-2: GRU network architecture
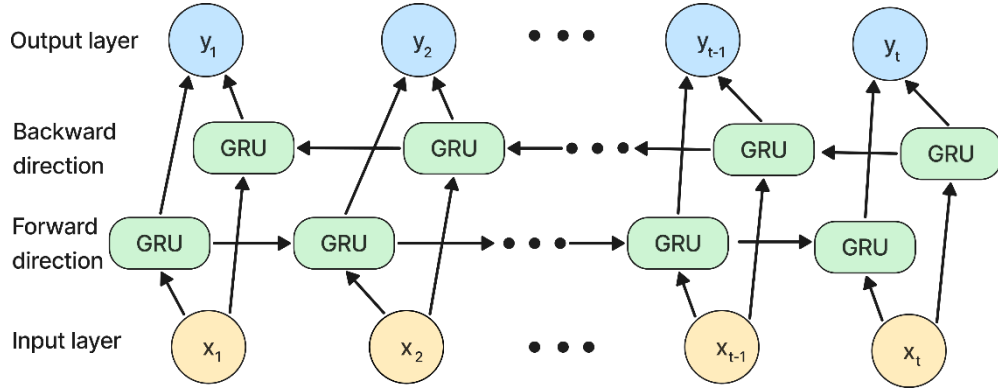
Figure 3-3: Bidirectional GRU network architecture

This bidirectional structure enables the model to extract richer degradation features from cycling data, improving the robustness and accuracy of SOH prediction. GRU eliminates the need for a separate memory cell by updating a hidden state directly, making it particularly efficient for SOH estimation from time-series sensor data. The GRU's reset and update gates can prevent gradient dispersion, guarantee long-term memory capacity, and lessen the model's computational load[49]. The update gate Z_t regulates the amount of the prior hidden state that is kept, helping to maintain long-term dependencies that are crucial for monitoring battery deterioration. The amount of historical data that is disregarded is determined by the reset gate R_t. While the final hidden state h_t integrates past and current information for efficient temporal representation, the candidate hidden state $\widehat{h}_t$ combines the reset-modulated memory and the current input. The sigmoid activation function is represented by σ, and the hyperbolic tangent activation function is represented by $tanh$, as shown in the equations below:

$$Z_t = \sigma(W_z \cdot [h_{t-1}, X_t]), \tag{3-9}$$

$$R_t = \sigma(W_r \cdot [h_{t-1}, X_t]), \tag{3-10}$$

$$\widehat{h}_t = tanh(W \cdot [R_t * h_{t-1}, X_t]), \tag{3-11}$$

$$h_t = (1 - Z_t) * h_{t-1} + Z_t * \widehat{h}_t, \tag{3-12}$$

$$\sigma = \frac{1}{1 + e^{-x}}, \tag{3-13}$$

$$tanh\,x = \frac{e^x - e^{-x}}{e^x + e^{-x}}. \tag{3-14}$$

3.2.3 Temporal attention for highlighting important time steps

The attention module conveys the temporal relevance of attributes and boosts the BiGRU's potential to learn detailed input-output links.   Relying on the most relevant parts of the input sequence is frequently vital in time-series modeling tasks, including battery SOH estimation. The temporal attention increases precision as well as understanding by enabling the model to select and attend to independent time steps through the distribution of important weights. The temporal attention suggested in [50], which has been tailored for time series data, strengthens neural networks' grasp in making use of the underlying trend patterns in these kinds of time series data. Because of this, time series data may be processed more precisely and individually. The basic temporal attention process for figuring out the SOH of LiBs comprises three stages: feature weighting, attention weight calculations, and SOH output generation [51] .

Given an input sequence $H = [h_1, h_2, \ldots, h_T] \in R^{T \times d}$, where T is the sequence length and d is the hidden dimension, the temporal attention computes attention weights α_t for each time step t as in:

$$e_t = tanh(W_a h_t + b_a), \tag{3-15}$$

$$\alpha_t = \frac{exp(e_t^\top u_a)}{\sum_{k=1}^{T} exp(e_k^\top u_a)} \tag{3-16}$$

where W_a and b_a are the weight and the bias matrix, and u_a is a vector that acts like a "query" to measure importance. They are all trainable parameters. The alignment score e_t represents the relevance of the hidden state h_t with respect to the overall sequence. The attention weights α_t are then normalized via the softmax function to ensure they sum to one. The final context vector c is computed as a weighted sum of the hidden states as shown below:

$$c = \sum_{t=1}^{T} \alpha_t h_t. \tag{3-17}$$

This context vector captures the most relevant temporal features and is subsequently passed to the output layer for final SOH estimation. The output of the model, representing the predicted SOH Y_{SOH}, is obtained through a function $f(c)$ that maps the context vector via a fully connected layer as in:

$$Y_{SOH} = f(c). \tag{3-18}$$

3.3 Model Execution process

The DL architecture presented in this research is as shown in figure 3-4. The proposed method includes 1D convolutional layers to capture local features from the time-series battery cycling data. Two 1D CNN layers act as an automatic feature extractor for training data, eliminating the need for manual feature extraction. These extracted local features pass through the BiGRU layer, capturing long-term dependencies. For resource-heavy tasks like utilizing time-series data of battery cycling to learn long-term dependencies, BiGRU layers have a better computational edge over BiLSTM layers. The learned long-term dependencies from the BiGRU layer pass through the temporal attention layer. The temporal attention layer is used to capture the most informative time steps in battery cycling time-series data while keeping the complexity of the model to a minimum. Finally, the output from the temporal attention layer is passed through the dense layer. The dense layer is the final layer in the proposed method, which reduces the higher dimensionality from other layers to one estimating SOH as the final output. The network is trained across 1000 epochs with a batch size of 16 and verified with LOOCV. Table 3-2 shows how the CALCE data are divided into four different groups for model training and testing. The proposed method is trained using the mean squared error loss function. The AdamW optimizer is employed with a learning rate of 0.001. A dropout of 0.25 is used during training to mitigate

overfitting by randomly deactivating a fraction of neurons in each iteration. Evaluation metrics such as MAE, RMSE, and R^2 are calculated on the test data for each group. General experimentation based on training loss and evaluation metrics is used to fine-tune hyperparameters.
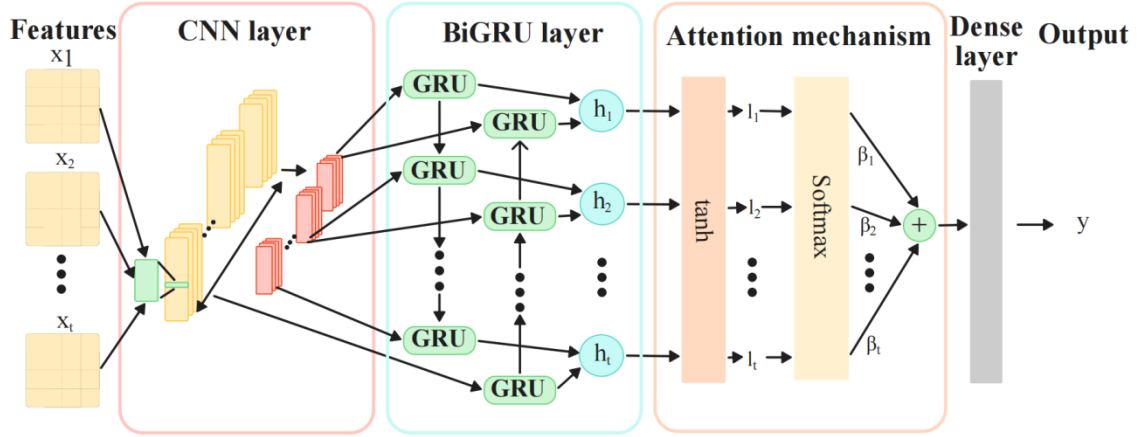
Figure 3-4: Full Process showing Execution of the Proposed Model. Feature matrices as input, CNN layer for feature extraction, BiGRU followed by temporal attention and dense layer for final output of SOH

TABLE 3-2: CALCE dataset CS2 cells battery training & testing groups

Group	Training Cells	Testing Cell
Group I	CS2_36, CS2_37, CS2_38	CS2_35
Group II	CS2_35, CS2_37, CS2_38	CS2_36
Group III	CS2_35, CS2_36, CS2_38	CS2_37
Group IV	CS2_35, CS2_36, CS2_37	CS2_38

3.4 Results and Discussion

The performance of different approaches for the SOH and RUL prediction is examined in this section. Four data groups were analyzed for training and testing. The SOH and RUL prediction results for every group are covered using performance evaluation metrics. The battery capacity in ampere-hours (Ah) is presented on the y-axis, and the cycle number is presented on the x-axis. A threshold of 70 % of the original capacity was used in this research to determine the EOL. In this research, RUL prediction started at the 400th cycle and ended at the EOL. The actual RUL values were then compared to five DL methods: CNN, LSTM, BiLSTM-GRU, CNN-BiLSTM, and the suggested CNN-BiGRU with the temporal attention. The black line indicates the true SOH, while the red line denotes the proposed method. The comparison of several models to estimate SOH and RUL on the group I is displayed in figure 3-5.
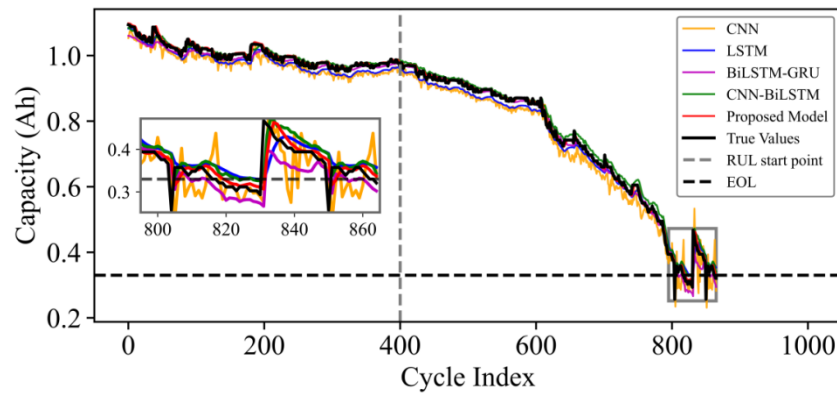
Figure 3-5: SOH and RUL prediction comparison of different models on CS2_35 cell

The comparison of prediction results utilizing multiple approaches is shown in Table 3-3. The proposed model achieved an MAE of 0.0072, RMSE of 0.0121, an R^2 of 0.9965 and an RUL_{error} of 2 cycles on group I of the dataset where CS2_35 cell is used for testing and other cells are used for training.

TABLE 3-3: CALCE dataset CS2_35 data group I prediction results

Model Name	SOH prediction			RUL Comparison		
	MAE	MAE	RMSE	MAE	RMSE	R^2
CNN	0.0269	0.0313	0.9770	404	420	16
LSTM	0.0180	0.0216	0.9891	404	419	15
BiLSTM-GRU	0.0125	0.0172	0.9930	404	416	12
CNN-BiLSTM	0.0116	0.0171	0.9931	404	414	10
Proposed	**0.0072**	**0.0121**	**0.9965**	**404**	**406**	**2**

Comparing the SOH and RUL predictions for group II, where CS2_36 is used as a testing cell and others are used for training, is shown in figure 3-6. The proposed method obtained the lowest SOH and RUL prediction error, with an SOH prediction MAE of 0.0082, an RMSE of 0.0145, and an RUL_{error} of 3 cycles, as shown in Table 3-4.
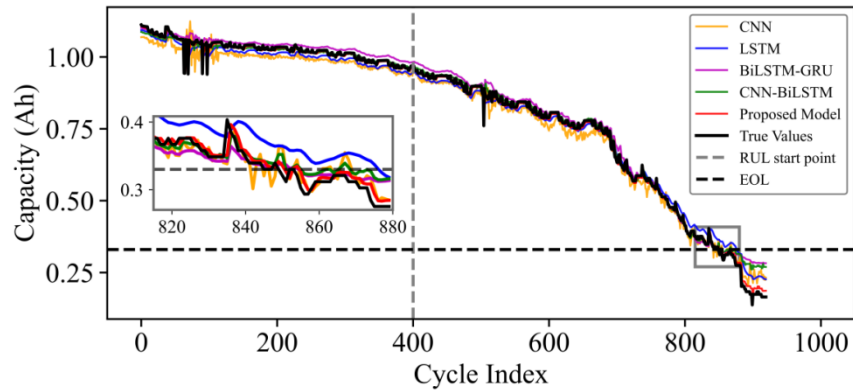
Figure 3-6: SOH prediction comparision of different models on CS2_36 cell

TABLE 3-4: CALCE dataset CS2_36 data group I prediction results

Model Name	SOH prediction			RUL Comparison		
	MAE	MAE	RMSE	MAE	RMSE	R^2
CNN	0.0264	0.0310	0.9855	450	463	13
LSTM	0.0208	0.0258	0.9900	450	457	7
BiLSTM-GRU	0.0131	0.0248	0.9910	450	455	5
CNN-BiLSTM	0.0199	0.0305	0.9859	450	442	8
Proposed	**0.0082**	**0.0145**	**0.9968**	**450**	**453**	**3**

Similarly, the proposed model's performance in group III of the dataset using CS_37 cell as the testing data is as shown in Figure 3-7.
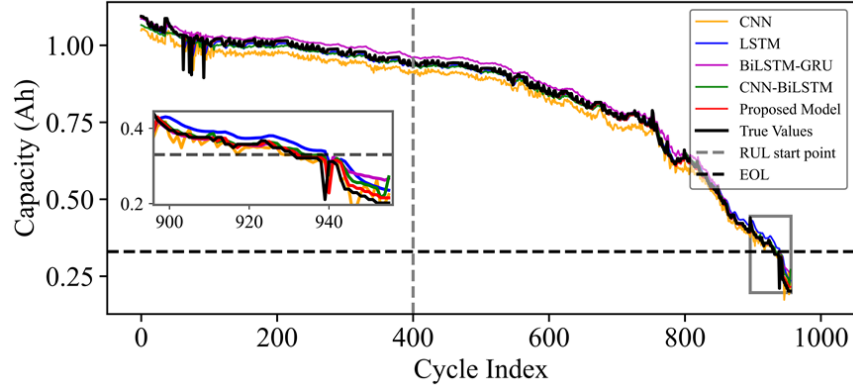
Figure 3-7: SOH prediction comparison of different models on CS2_37 cell

The comparative error analysis of multiple models using the CS2_37 cell's data for testing   is as shown in Table 3-5. The proposed method obtained good results, with an MAE of 0.0065, an RMSE of 0.0124, an R^2 of 0.9963, and an RUL_{error} of 1 cycle in group III, where the CS2_37 cell's data is used for testing and other cells' data are used for training.

TABLE 3-5: CALCE dataset CS2_37 data group I prediction results

Model Name	SOH prediction			RUL Comparison		
	MAE	MAE	RMSE	MAE	RMSE	R^2
CNN	0.0297	0.0321	0.9759	532	551	19
LSTM	0.0112	0.0216	0.9941	532	537	5
BiLSTM-GRU	0.0110	0.0172	0.9944	532	536	4
CNN-BiLSTM	0.0173	0.0215	0.9891	532	541	9
Proposed	**0.0065**	**0.0124**	**0.9963**	**532**	**533**	**1**

Similarly, the SOH and RUL predictions of various models were graphically compared for group IV of the dataset, where CS_38 cell is used as testing and other cells are used for training as shown in figure 3-8, and evaluation metrics were compared in table 3-6. Our model scored exceptionally well in SOH and RUL prediction with an MAE of 0.0075, an RMSE of 0.0131, an R^2 of 0.9958, and an RUL_{error} of 0 cycle.
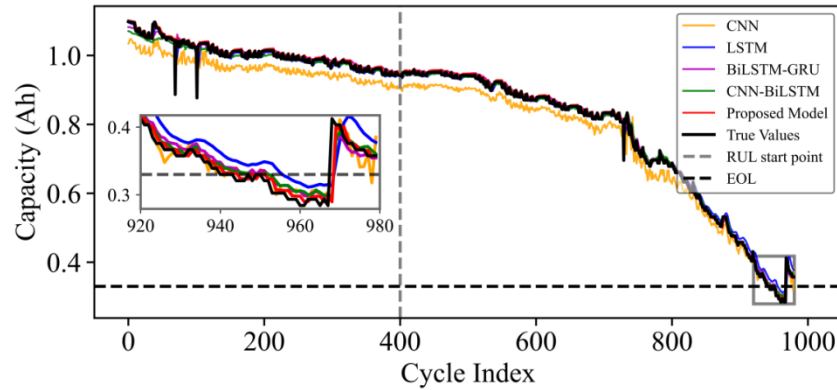
Figure 3-8: SOH prediction comparison of different models on CS2_38 cell

TABLE 3-6: CALCE dataset CS2_38 data group I prediction results

Model Name	SOH prediction			RUL Comparison		
	MAE	MAE	RMSE	MAE	RMSE	R^2
CNN	0.0264	0.0368	0.9671	540	553	13
LSTM	0.0095	0.0149	0.9946	540	547	7
BiLSTM-GRU	0.0083	0.0133	0.9956	540	550	10
CNN-BiLSTM	0.0084	0.0134	0.9856	540	548	8
Proposed	**0.0075**	**0.0131**	**0.9958**	**540**	**540**	**0**

4 IPEformer experiments and analysis

4.1 Dataset descriptions

In this research, we use four datasets CALCE CS2-type battery dataset [52], NASA Prognostics Center of Excellence battery dataset [53], Toyota-MIT-Stanford dataset [54] and Xi'an Jiaotong University (XJTU) battery dataset [55].

CALCE dataset consists of four prismatic CS2 cells, each cell's rated capacity is 1100 mAh. The dataset was collected using constant current (CC) and constant voltage (CV) charging and discharging protocol.

The CC of 0.55 amperes (A) is applied to charge the battery until its voltage reach maximum cutoff of 4.2 volts (V) and then 4.2 V was sustained until the charging current dropped to below 50 milliamperes (mA). In discharging CC of 1.1 A is applied until their voltage reach below 2.7 V. More technical information of the CALCE dataset is given in Table 4-1.
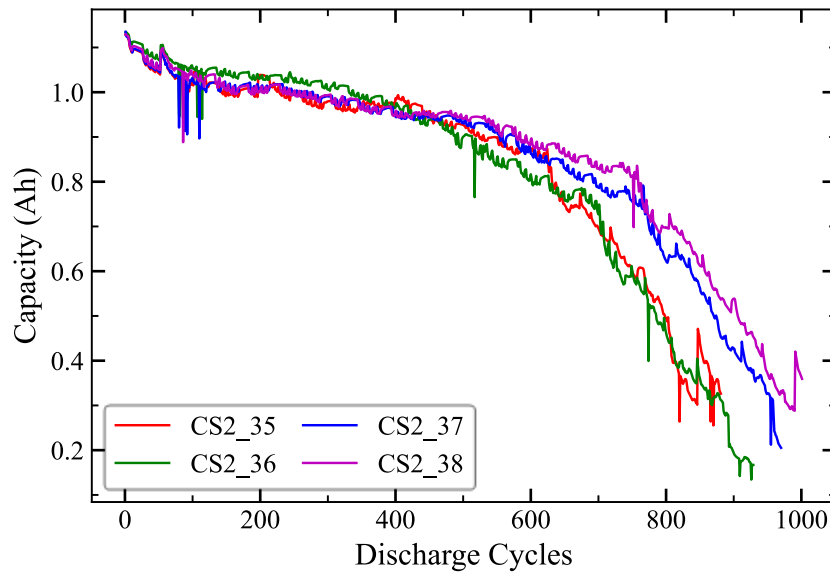
Figure 4-1: Capacity degradation plot of CALCE dataset
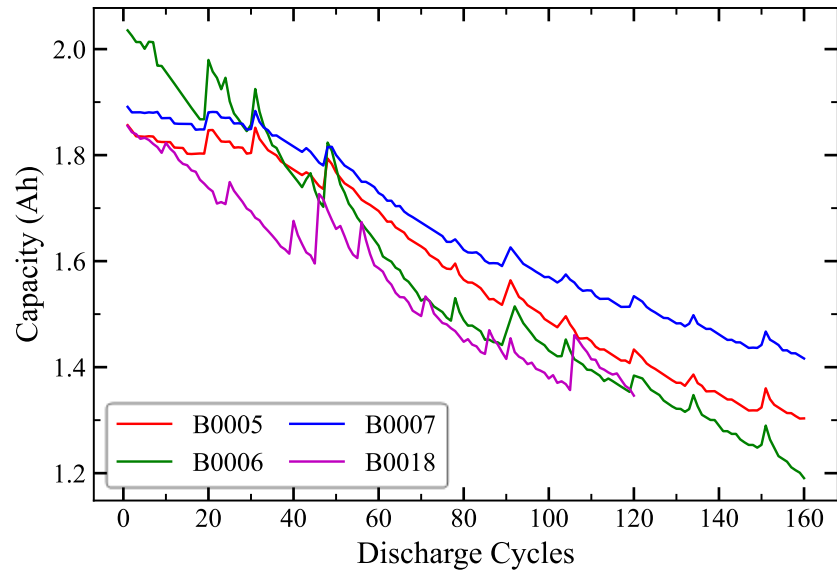
Figure 4-2: Capacity degradation plot of first batch of NASA dataset
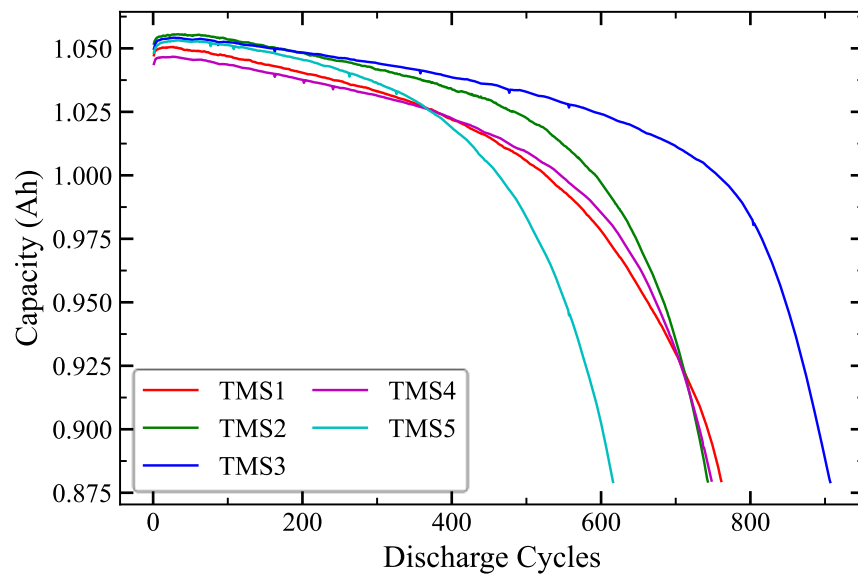
Figure 4-3: Capacity degradation plot of first batch of Toyota-MIT-Stanford dataset
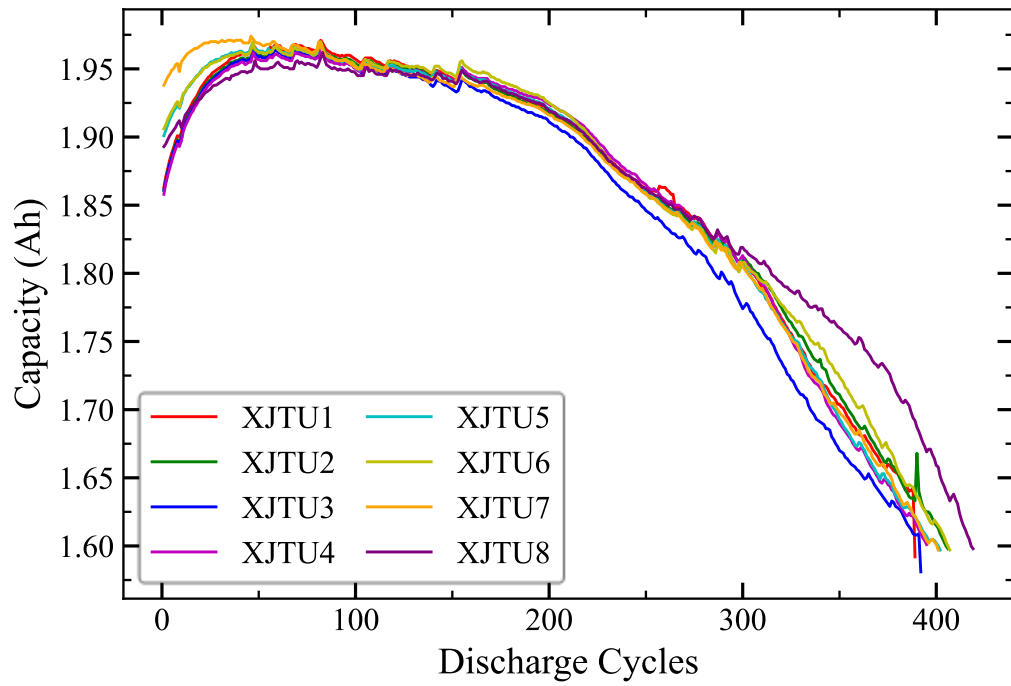
Figure 4-4: Capacity degradation plot of first batch of XJTU dataset
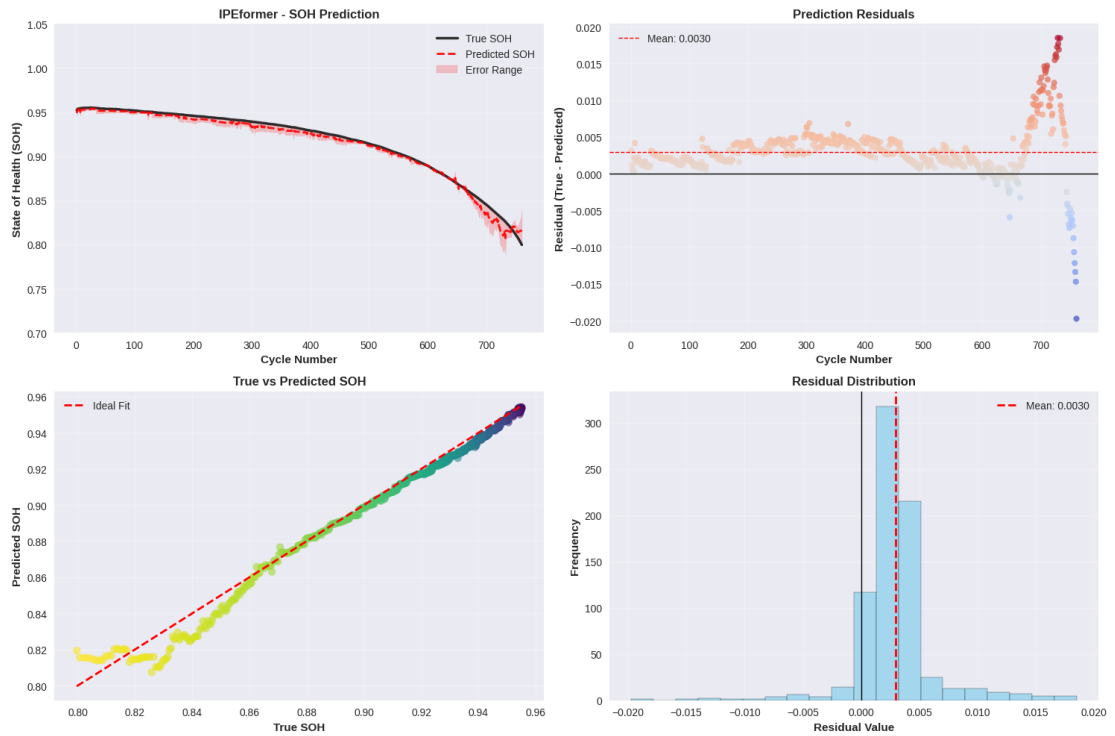
Figure 4-5: Preliminary experimental results on Cell-1 using MIT group-1 dataset trained on IPEformer
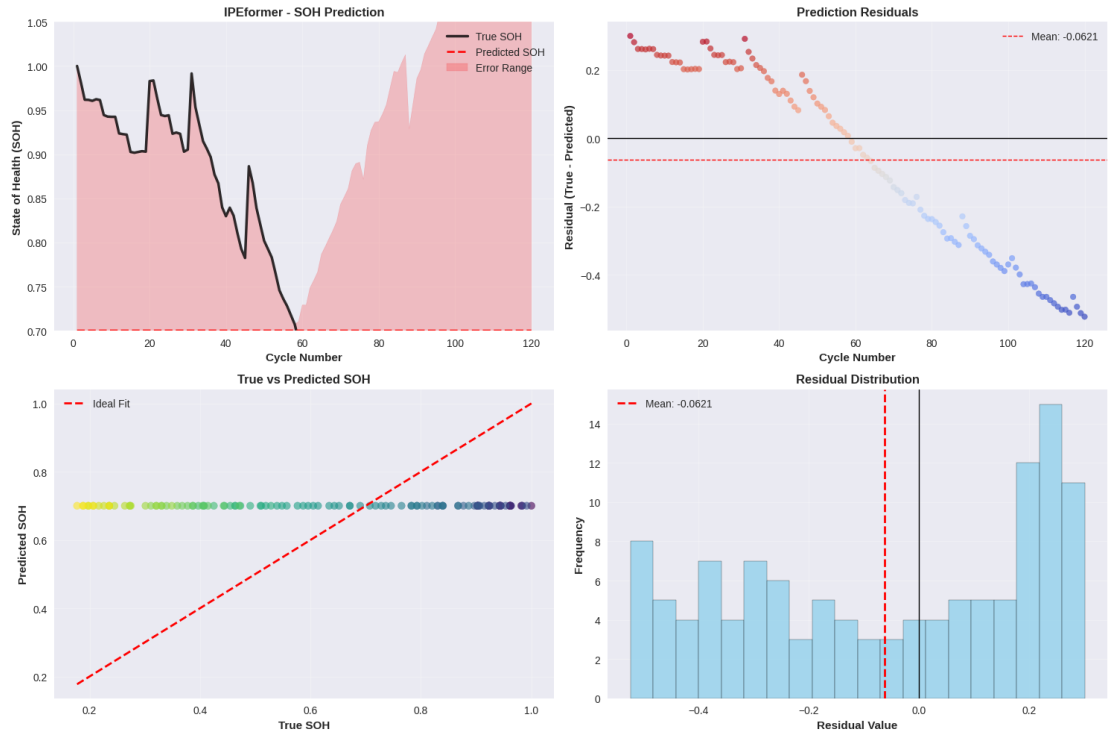
Figure 4-6: Preliminary experimental results on B0005 cell of NASA dataset trained on IPEformer
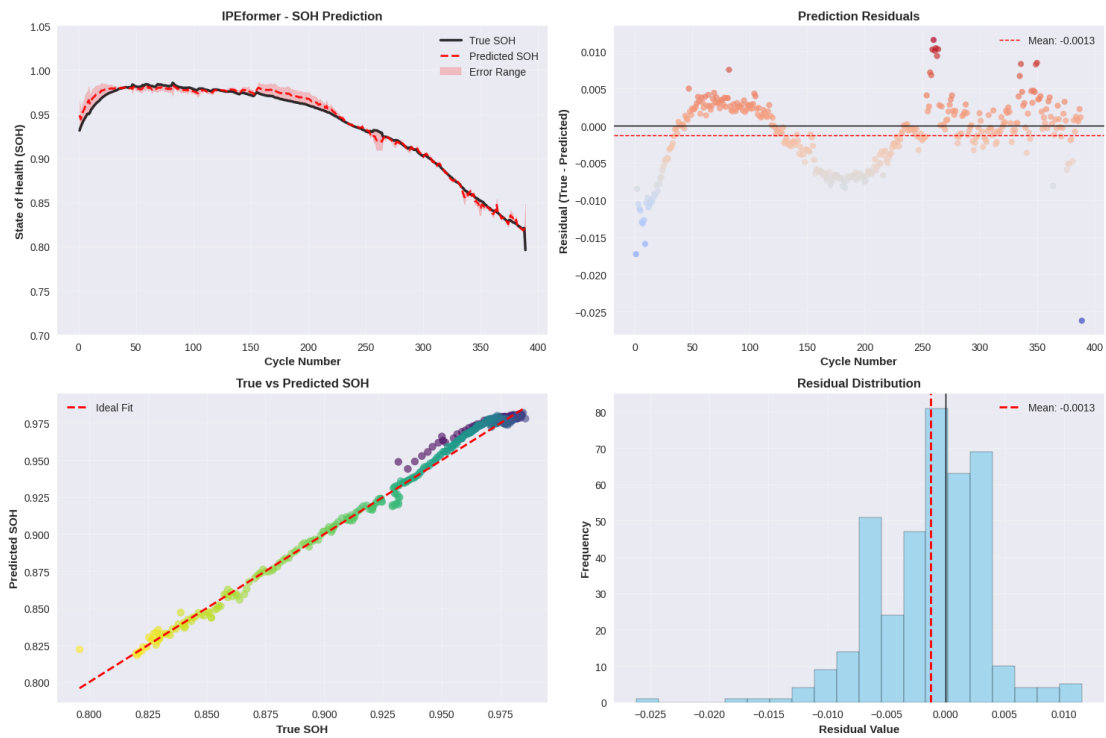
Figure 4-7: Preliminary experimental results on Cell1 of XJTU batch-1 dataset trained on IPEformer
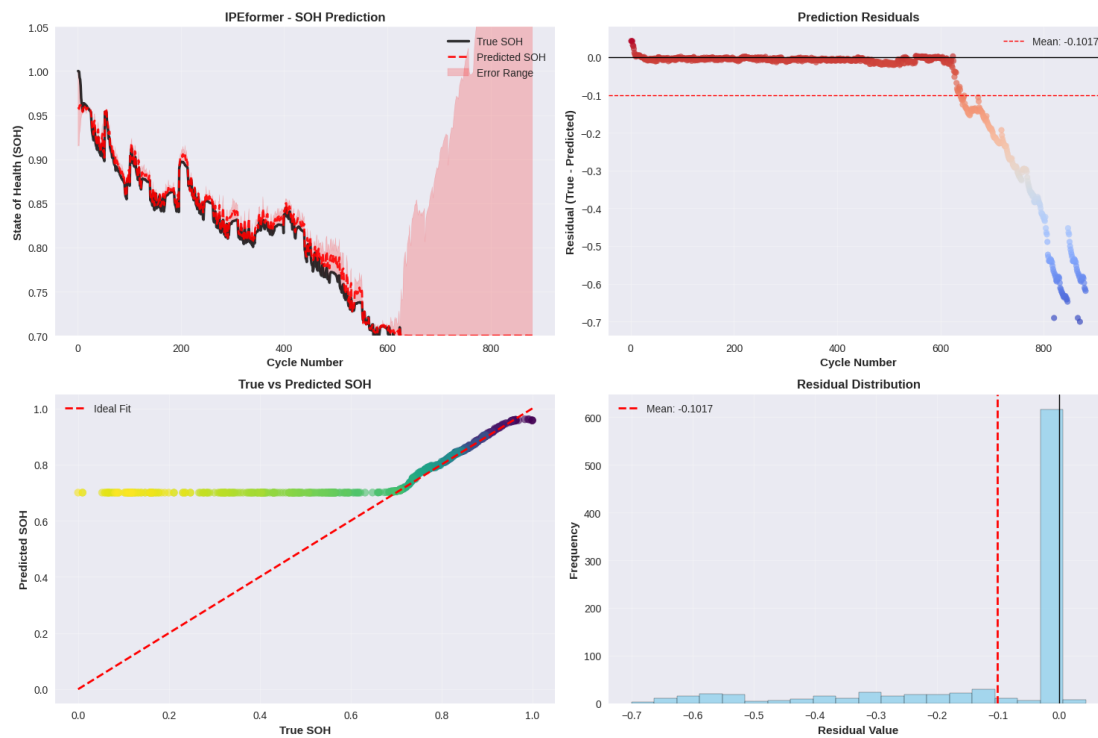
Figure 4-8: Preliminary experimental results on CS2_35 of CALCE dataset trained on IPEformer

5 Preliminary Experimental Results

5.1 Datasets descriptions

The 350 mAh Pouch Cells battery dataset consists of five pouch Li-ion cells, each with a rated capacity of 350 mAh. Charging is performed with a constant current (CC) of 175 mA until the voltage reaches 4.2 V, followed by a constant voltage (CV) phase at 4.2 V until the charging current drops to 5 mA. Discharging is carried out at a constant current of 350 mA until the voltage drops to 2.75 V. Table 1 summarizes the technical specifications of the 350 mAh Pouch Cells dataset.

The dataset comprises four 2200 mAh cylindrical-type lithium-ion cells (Cell1–Cell4) with nominal dimensions of 18×65 mm. Charging starts with a constant current of 1.1 A until the voltage reaches 4.2 V, followed by a constant voltage phase at 4.2 V until the charging current drops to 22 mA. Discharging is performed at a constant current of 2.2 A until the voltage drops to 2.75 V. Four batteries—Cell1, Cell2, Cell3, and Cell4—are selected from the dataset for this research work. The battery is considered to have reached its end of life (EOL) when its capacity fades by 30 %, i.e., from 2200 mAh to 1540 mAh. Table 1 summarizes the technical specifications of the 2200 mAh Cylindrical Cells dataset.

Parameter	350 mAh Pouch Cells	2200 mAh Cylindrical (18650) Cells
Cells used	Cell1, Cell2, Cell3, Cell4, Cell5	Cell1, Cell2, Cell3, Cell4
Form factor	Pouch	Cylindrical (18×65 mm)
Dimensions	35×20×5 mm (± tolerances)	Ø 18.3 ± 2 mm, Height 67 ± 2 mm
Weight	6 g	44 g
Rated capacity	350 mAh	2200 mAh
EOL capacity (30 % fade)	245 mAh	1540 mAh
Charging current	0.5C (175 mA) → CV at 4.2 V until 5 mA	0.5C (1.1 A) → CV at 4.2 V until 22 mA
Discharging current	1C (350 mA)	1C (2.2 A)
Charging protocol	CC-CV	CC-CV
Discharging protocol	CC	CC
Nominal voltage	3.7 V	3.7 V
Charge cut-off voltage	4.2 V	4.2 V
Discharge cut-off voltage	2.75 V	2.75 V
Rated charging temperature	10–45 °C	10–45 °C
Rated discharging temperature	–10–80 °C	–10–55 °C
Rated cycle life	500–800 cycles	300–500 cycles

Figure 5-1 Experimental setup for battery cycling data collection for 2200 mAh Cylindrical and 350 mAh Pouch cells

5.2 Battery Cycling experimental results
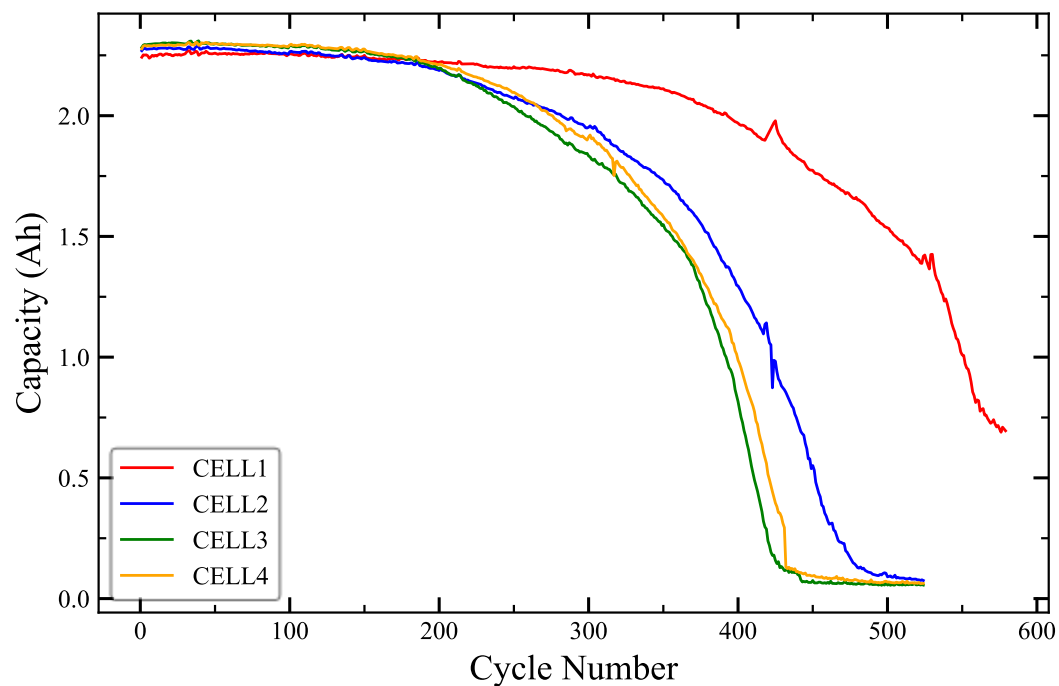
Figure 5-1: Capacity degradation plot of 2200 mAh dataset
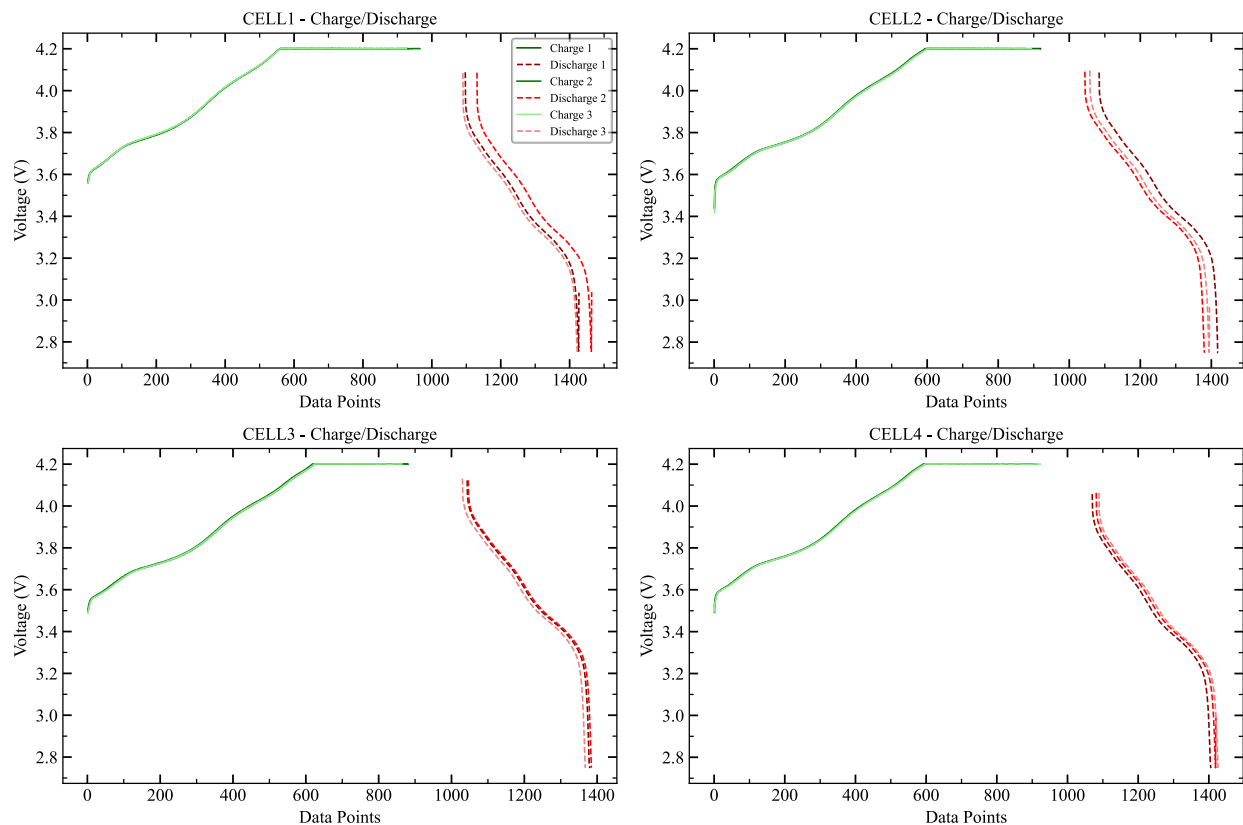
Figure 5-2: Charge-discharge voltage plot of 2200 mAh battery dataset
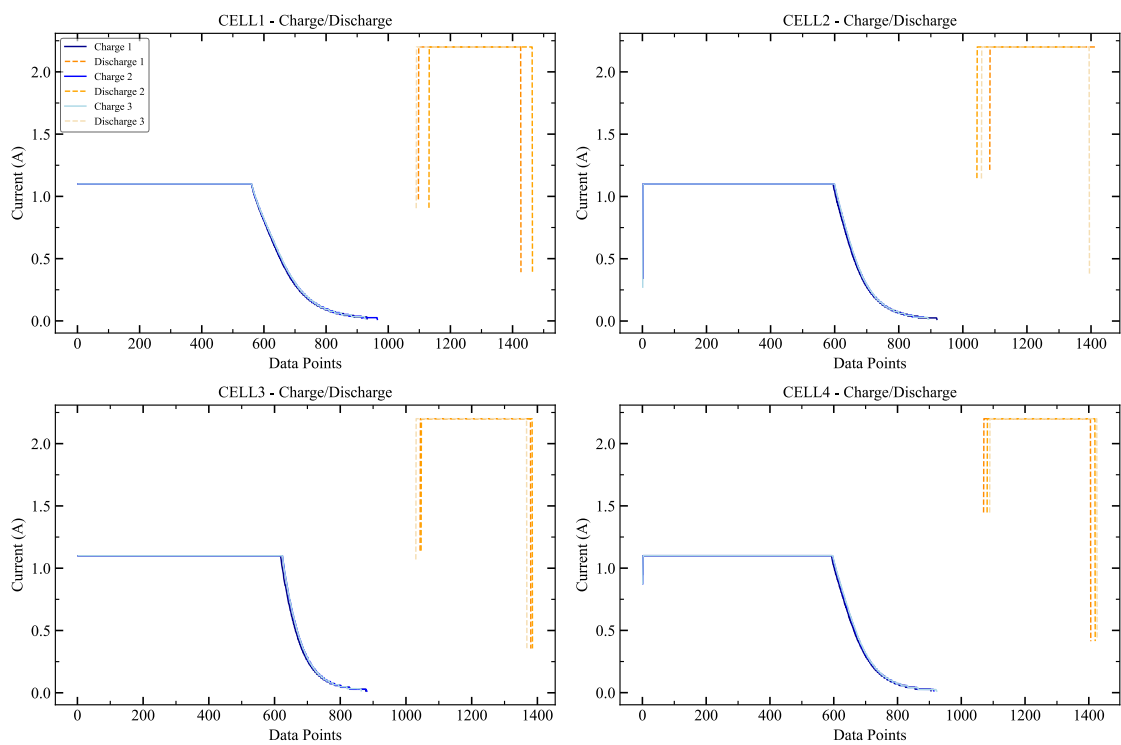
Figure 5-3: Charge-discharge current plot of 2200 mAh battery dataset
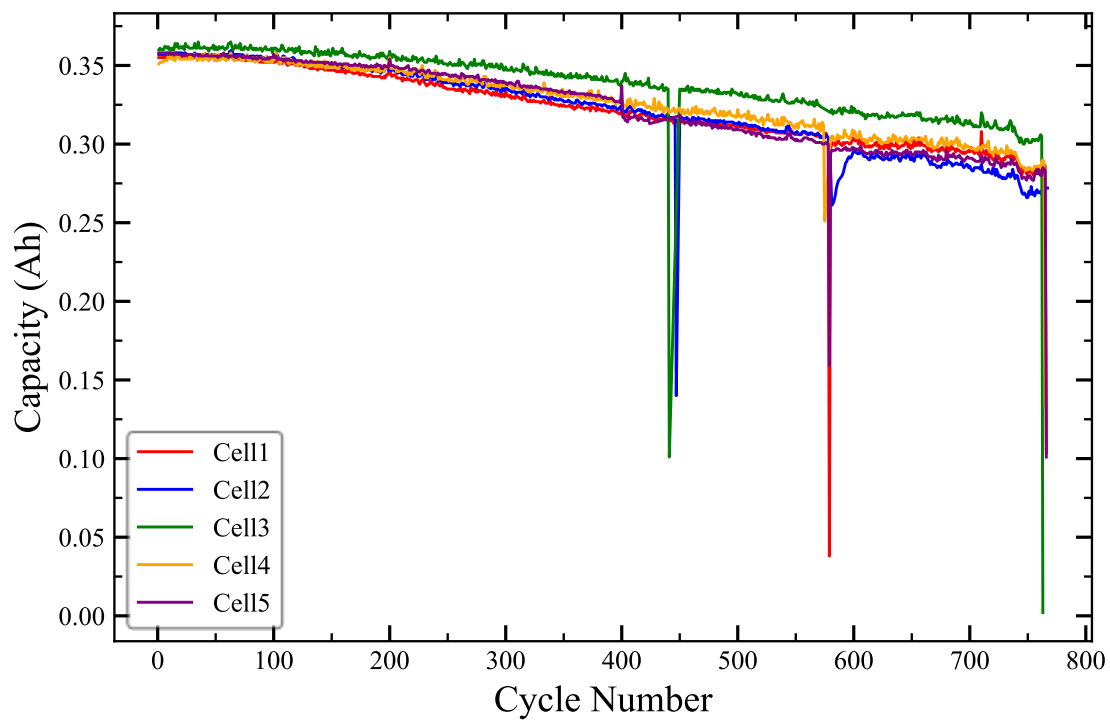
Figure 5-2: Capacity degradation plot of 350 mAh dataset
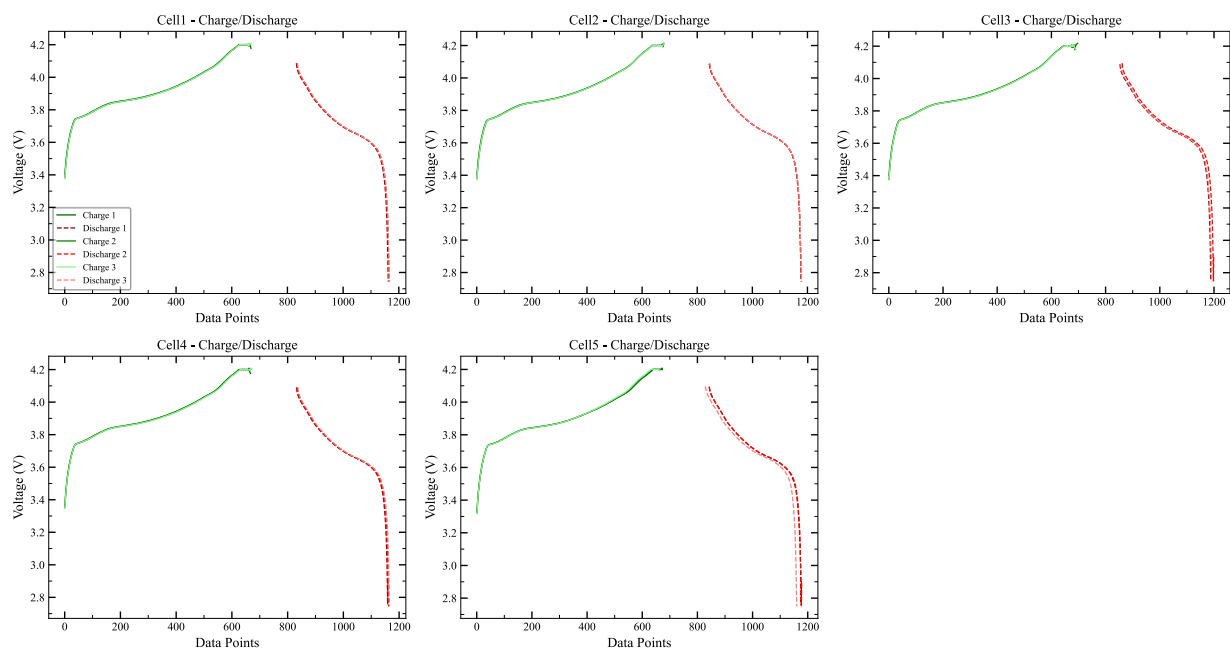
Figure 5-2: Charge-discharge voltage plot of 350 mAh dataset
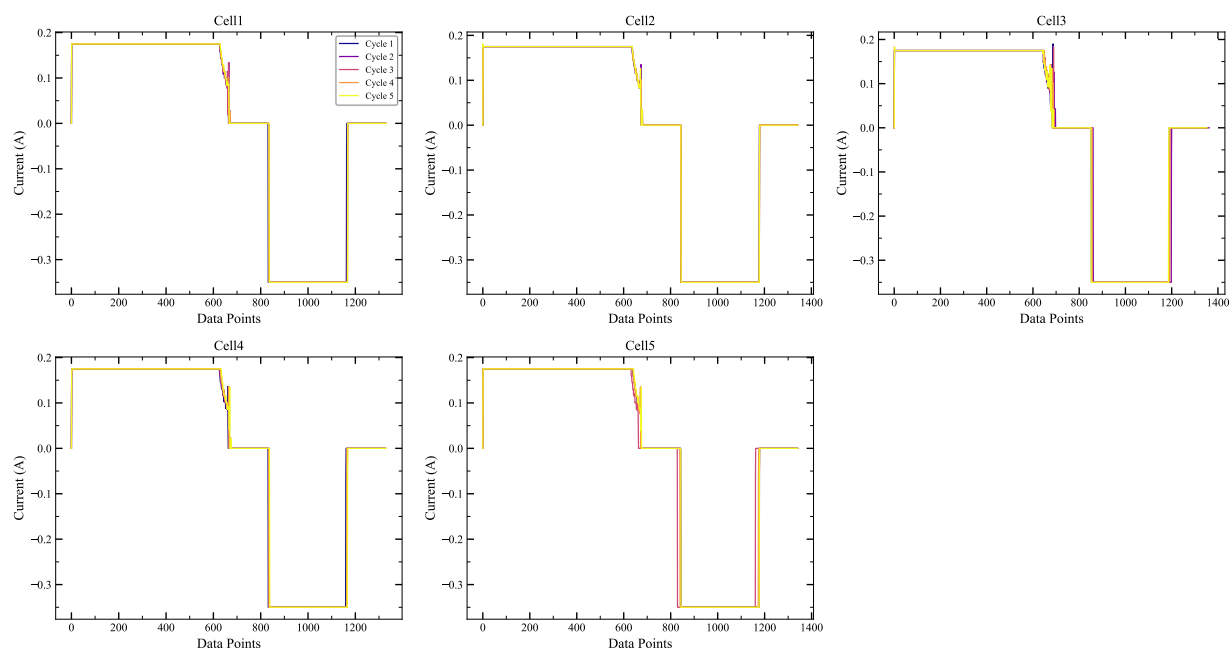
Figure 5-2: Charge-discharge current plot of 350 mAh dataset

二、哪些研究内容未按计划完成，原因何在？

The research content has not completed as planned, and the reason

The following research tasks have not been completed according to the original schedule:

1. Achieving SOH estimation performance clearly superior to the current state-of-the-art on all four public datasets (NASA, MIT-Stanford, CALCE, XJTU).
   - Reason: Greater-than-expected difficulty in surpassing literature baselines; extensive time was required for data preprocessing, health-indicator selection/construction, and experimentation with numerous deep-learning architectures.
2. Thorough analysis and performance optimization specifically on the NASA randomized dataset.
   - Reason: The NASA dataset exhibits higher complexity and noise; the current data loader, preprocessing pipeline, and training strategy need significant redesign and additional in-depth analysis to yield competitive results.
3. Completion of the laboratory battery cycling experiment for collecting real-world degradation data.
   - Reason: The physical cycling tests (especially long-term degradation tests under multiple operating conditions) have progressed slower than anticipated due to equipment scheduling, battery cell variability, and the need for repeated validation measurements.
   - Current progress: Approximately 80% completed. The remaining 20% (final cycles under extreme conditions and verification tests) is expected to require an additional 1 month (completion targeted for late December 2025). After data collection, post-processing, analysis, and integration into the model validation will be carried out immediately, and a dedicated journal paper summarizing the experimental dataset and preliminary findings will be prepared in parallel.

Despite these delays, no fundamental obstacles have been encountered, and all unfinished tasks remain fully achievable within the adjusted timeline.

三、存在的问题和需要说明的情况（调整变动内容）
The existing problems, and the situation needed to explain (revise or change research content)

The main reasons certain research tasks were not completed according to the original plan are as follows:
- Encountered greater-than-expected difficulty in obtaining results that clearly outperform the current state-of-the-art methods reported in the literature.
- A significant amount of time was spent on data preprocessing, health-indicator construction/selection, and extensive experiments with various deep-learning architectures for SOH estimation on four public datasets (NASA, MIT-Stanford, CALCE, and XJTU).
- The NASA dataset proved particularly challenging; the current data loader and training pipeline need substantial improvement and more thorough analysis to achieve competitive performance.

Due to the above issues, the following adjustments to the original research plan are proposed:
- Slightly extend the experimental validation phase for the NASA dataset (additional 1–2 months).
- Shift partial focus from developing entirely new architectures to enhanced feature engineering and model optimization of the existing IPEformer framework, while still aiming to surpass literature baselines on all datasets.
- No major change to the overall research objectives, but the timeline for final comparative results and paper submission will be postponed accordingly.

四、后续研究工作安排
The next research work arrangement

The follow-up research work for the remaining period is planned as follows:

- Perform targeted feature extraction and health-indicator optimization for the NASA, MIT-Stanford, CALCE, and XJTU datasets before final model training.
- Further improve the IPEformer model (architecture refinement, loss function design, attention mechanism optimization, etc.) to achieve higher accuracy and ensure it outperforms existing state-of-the-art models on at least three of the four datasets.
- Conduct systematic hyperparameter tuning (learning rate, batch size, dropout, transformer layers/depth, etc.) and ablation studies.
- Complete all remaining experiments, organize comparative results, and finish writing the journal manuscript.
- Expected completion timeline: core experiments concluded by the end of January 2026; full paper submitted by March 2026.

4 References

[1] J. L. Holechek, H. M. E. Geli, M. N. Sawalhah, and R. Valdez, "A Global Assessment: Can Renewable Energy Replace Fossil Fuels by 2050?," *Sustainability*, vol. 14, no. 8, p. 4792, Apr. 2022, doi: 10.3390/su14084792.

[2] Akinwale Ishola, "Global renewable energy transition in fossil fuel dependent regions," *World J. Adv. Res. Rev.*, vol. 24, no. 1, pp. 1373–1380, Oct. 2024, doi: 10.30574/wjarr.2024.24.1.3046.

[3] V. Powar and R. Singh, "End-to-End Direct-Current-Based Extreme Fast Electric Vehicle Charging Infrastructure Using Lithium-Ion Battery Storage," *Batteries*, vol. 9, no. 3, p. 169, Mar. 2023, doi: 10.3390/batteries9030169.

[4] J. Suvvala, S. K. K, C. Dhananjayulu, H. Kotb, and A. Elrashidi, "Integration of renewable energy sources using multiport converters for ultra-fast charging stations for electric vehicles: An overview," *Heliyon*, vol. 10, no. 15, p. e35782, Aug. 2024, doi: 10.1016/j.heliyon.2024.e35782.

[5] H. Naseem, A. Hadi, M. Kang, and J. Seok, "Enhancing Energy Storage Efficiency: Advances in Battery Management Systems in Electric Vehicles," *Energy Technol.*, vol. 13, no. 8, p. 2500100, Aug. 2025, doi: 10.1002/ente.202500100.

[6] M. S. Hossain Lipu *et al.*, "Intelligent algorithms and control strategies for battery management system in electric vehicles: Progress, challenges and future outlook," *J. Clean. Prod.*, vol. 292, p. 126044, Apr. 2021, doi: 10.1016/j.jclepro.2021.126044.

[7] A. T. P. Zau, M. J. Lencwe, S. P. D. Chowdhury, and T. O. Olwal, "A Battery Management Strategy in a Lead-Acid and Lithium-Ion Hybrid Battery Energy Storage System for Conventional Transport Vehicles," *Energies*, vol. 15, no. 7, p. 2577, Apr. 2022, doi: 10.3390/en15072577.

[8] S. Nazaralizadeh, P. Banerjee, A. K. Srivastava, and P. Famouri, "Battery Energy Storage Systems: A Review of Energy Management Systems and Health Metrics," *Energies*, vol. 17, no. 5, p. 1250, Mar. 2024, doi: 10.3390/en17051250.

[9] Z. Liao, S. Zhang, K. Li, G. Zhang, and T. G. Habetler, "A survey of methods for monitoring and detecting thermal runaway of lithium-ion batteries," *J. Power Sources*, vol. 436, p. 226879, Oct. 2019, doi: 10.1016/j.jpowsour.2019.226879.

[10] L. Schmidt, K. Hankins, L. Bläubaum, M. Gerasimov, and U. Krewer, "High temperature *in situ* gas analysis for identifying degradation mechanisms of lithium-ion batteries," *Chem. Sci.*, vol. 16, no. 12, pp. 5118–5128, 2025, doi: 10.1039/D4SC08105F.

[11] P. Prochazka, D. Cervinka, J. Martis, R. Cipin, and P. Vorel, "Li-Ion Battery Deep Discharge Degradation," *ECS Trans.*, vol. 74, no. 1, pp. 31–36, Dec. 2016, doi: 10.1149/07401.0031ecst.

[12] A. K. M. A. Habib, M. K. Hasan, G. F. Issa, D. Singh, S. Islam, and T. M. Ghazal, "Lithium-Ion Battery Management System for Electric Vehicles: Constraints, Challenges, and Recommendations," *Batteries*, vol. 9, no. 3, p. 152, Feb. 2023, doi: 10.3390/batteries9030152.

[13] Y. Chen, "Recent advances of overcharge investigation of lithium-ion batteries," *Ionics*, vol. 28, no. 2, pp. 495–514, Feb. 2022, doi: 10.1007/s11581-021-04331-3.

[14] R. Venkatasatish and C. Dhanamjayulu, "Design and implementation of an inductor based cell balancing circuit with reduced switches for Lithium-ion batteries," *Sci. Rep.*, vol. 14, no. 1, p. 28691, Nov. 2024, doi: 10.1038/s41598-024-80096-9.

[15] A. Ashraf *et al.*, "Review of Cell-Balancing Schemes for Electric Vehicle Battery Management Systems,"

Energies, vol. 17, no. 6, p. 1271, Mar. 2024, doi: 10.3390/en17061271.

[16] N. Collath, B. Tepe, S. Englberger, A. Jossen, and H. Hesse, "Aging aware operation of lithium-ion battery energy storage systems: A review," *J. Energy Storage*, vol. 55, p. 105634, Nov. 2022, doi: 10.1016/j.est.2022.105634.

[17] S. S. Madani *et al.*, "A Comprehensive Review on Lithium-Ion Battery Lifetime Prediction and Aging Mechanism Analysis," *Batteries*, vol. 11, no. 4, p. 127, Mar. 2025, doi: 10.3390/batteries11040127.

[18] D. Shi *et al.*, "A review of the combined effects of environmental and operational factors on lithium-ion battery performance: temperature, vibration, and charging/discharging cycles," *RSC Adv.*, vol. 15, no. 17, pp. 13272–13283, 2025, doi: 10.1039/D5RA00934K.

[19] C. A. Rufino Júnior *et al.*, "Unraveling the Degradation Mechanisms of Lithium-Ion Batteries," *Energies*, vol. 17, no. 14, p. 3372, July 2024, doi: 10.3390/en17143372.

[20] D. Ansean *et al.*, "Lithium-Ion Battery Degradation Indicators Via Incremental Capacity Analysis," *IEEE Trans. Ind. Appl.*, vol. 55, no. 3, pp. 2992–3002, May 2019, doi: 10.1109/TIA.2019.2891213.

[21] F. Wang, Z. Zhai, Z. Zhao, Y. Di, and X. Chen, "Physics-informed neural network for lithium-ion battery degradation stable modeling and prognosis," *Nat. Commun.*, vol. 15, no. 1, p. 4332, May 2024, doi: 10.1038/s41467-024-48779-z.

[22] B. Yang *et al.*, "Research on Degradation Characteristics and Real-Time Reliability Assessment of Lithium-Ion Batteries," *J. Electrochem. Soc.*, vol. 172, no. 6, p. 060519, June 2025, doi: 10.1149/1945-7111/ade128.

[23] M. Wu *et al.*, "State of Health Estimation and Remaining Useful Life Prediction of Lithium-Ion Batteries by Charging Feature Extraction and Ridge Regression," *Appl. Sci.*, vol. 14, no. 8, p. 3153, Apr. 2024, doi: 10.3390/app14083153.

[24] E. Kim and S. Jung, "Battery State of Health Estimation Methods: Implementation and Comparison of 11 Algorithms," *IEEE Access*, vol. 13, pp. 55599–55615, 2025, doi: 10.1109/ACCESS.2025.3541631.

[25] B. Routh, A. Guha, S. Mukhopadhyay, and A. Patra, "Online Co-Estimation of the State-of-Health, State-of-Charge, and Remaining-Useful-Life of Lithium-Ion Batteries Using a Discrete Capacity Loss Model," *IEEE Trans. Transp. Electrification*, vol. 11, no. 2, pp. 6962–6975, Apr. 2025, doi: 10.1109/TTE.2024.3521316.

[26] X. Sun, Y. Zhang, Y. Zhang, L. Wang, and K. Wang, "Summary of Health-State Estimation of Lithium-Ion Batteries Based on Electrochemical Impedance Spectroscopy," *Energies*, vol. 16, no. 15, p. 5682, July 2023, doi: 10.3390/en16155682.

[27] E. Cabrera-Castillo, F. Niedermeier, and A. Jossen, "Calculation of the state of safety (SOS) for lithium ion batteries," *J. Power Sources*, vol. 324, pp. 509–520, Aug. 2016, doi: 10.1016/j.jpowsour.2016.05.068.

[28] S. Tao *et al.*, "Generative learning assisted state-of-health estimation for sustainable battery recycling with random retirement conditions," *Nat. Commun.*, vol. 15, no. 1, p. 10154, Nov. 2024, doi: 10.1038/s41467-024-54454-0.

[29] Y. Liu, C. Liu, Y. Liu, F. Sun, J. Qiao, and T. Xu, "Review on degradation mechanism and health state estimation methods of lithium-ion batteries," *J. Traffic Transp. Eng. Engl. Ed.*, vol. 10, no. 4, pp. 578–610, Aug. 2023, doi: 10.1016/j.jtte.2023.06.001.

[30] L. Zhang, L. Liu, A. Terekhov, D. Warnberg, and P. Zhao, "Thermal runaway of Li-ion battery with different aging histories," *Process Saf. Environ. Prot.*, vol. 185, pp. 910–917, May 2024, doi: 10.1016/j.psep.2024.03.077.

[31] G. Roe, "Air Busan Fire Highlights Lithium-Ion Battery Risks in Air Travel," Aviacionline. Accessed: Jan. 01, 2025. [Online]. Available: https://www.aviacionline.com/air-busan-fire-highlights-lithium-ion-battery-risks-in-air-travel

[32] M. Taouk, "Five cars destroyed at Sydney Airport after EV battery explosion," *ABC News*, Sept. 2023, [Online]. Available: https://www.abc.net.au/news/2023-09-12/sydney-airport-lithium-ion-battery-causes-

fire/102846146

[33] S. Singh, R. K. Saket, and B. Khan, "A comprehensive state-of-the-art review on reliability assessment and charging methodologies of grid-integrated electric vehicles," *IET Electr. Syst. Transp.*, vol. 13, no. 1, p. e12073, Mar. 2023, doi: 10.1049/els2.12073.

[34] M. Elmahallawy, T. Elfouly, A. Alouani, and A. M. Massoud, "A Comprehensive Review of Lithium-Ion Batteries Modeling, and State of Health and Remaining Useful Lifetime Prediction," *IEEE Access*, vol. 10, pp. 119040–119070, 2022, doi: 10.1109/ACCESS.2022.3221137.

[35] O. Demirci, S. Taskin, E. Schaltz, and B. Acar Demirci, "Review of battery state estimation methods for electric vehicles-Part II: SOH estimation," *J. Energy Storage*, vol. 96, p. 112703, Aug. 2024, doi: 10.1016/j.est.2024.112703.

[36] S. G. Padder *et al.*, "Data-Driven Approaches for Estimation of EV Battery SoC and SoH: A Review," *IEEE Access*, vol. 13, pp. 35048–35067, 2025, doi: 10.1109/ACCESS.2025.3539528.

[37] P. Iurilli, C. Brivio, R. E. Carrillo, and V. Wood, "Physics-Based SoH Estimation for Li-Ion Cells," *Batteries*, vol. 8, no. 11, p. 204, Nov. 2022, doi: 10.3390/batteries8110204.

[38] I. Lopetegi, G. L. Plett, M. S. Trimboli, L. Oca, E. Miguel, and U. Iraola, "A New Battery SOC/SOH/eSOH Estimation Method Using a PBM and Interconnected SPKFs: Part II. SOH and eSOH Estimation," *J. Electrochem. Soc.*, vol. 171, no. 3, p. 030518, Mar. 2024, doi: 10.1149/1945-7111/ad30d5.

[39] Z. Liu, J. Zhao, H. Wang, and C. Yang, "A New Lithium-Ion Battery SOH Estimation Method Based on an Indirect Enhanced Health Indicator and Support Vector Regression in PHMs," *Energies*, vol. 13, no. 4, p. 830, Feb. 2020, doi: 10.3390/en13040830.

[40] L. Qian, L. Xuan, and J. Chen, "Battery SOH estimation based on decision tree and improved support vector machine regression algorithm," *Front. Energy Res.*, vol. 11, p. 1218580, June 2023, doi: 10.3389/fenrg.2023.1218580.

[41] W. Duan, S. Song, F. Xiao, Y. Chen, S. Peng, and C. Song, "Battery SOH estimation and RUL prediction framework based on variable forgetting factor online sequential extreme learning machine and particle filter," *J. Energy Storage*, vol. 65, p. 107322, Aug. 2023, doi: 10.1016/j.est.2023.107322.

[42] C. Zhang *et al.*, "Battery SOH estimation method based on gradual decreasing current, double correlation analysis and GRU," *Green Energy Intell. Transp.*, vol. 2, no. 5, p. 100108, Oct. 2023, doi: 10.1016/j.geits.2023.100108.

[43] X. Huang, J. Wei, J. Huang, Q. Zhang, R. Zhong, and R. Lai, "Enhanced Lithium-Ion Battery SOH Estimation Using Bayesian-Optimized CNN Deep Learning Approach," *Int. J. Pattern Recognit. Artif. Intell.*, vol. 38, no. 11, p. 2452020, Sept. 2024, doi: 10.1142/S0218001424520207.

[44] J. Huang *et al.*, "A lithium-ion battery SOH estimation method based on temporal pattern attention mechanism and CNN-LSTM model," *Comput. Electr. Eng.*, vol. 122, p. 109930, Mar. 2025, doi: 10.1016/j.compeleceng.2024.109930.

[45] R. Zheng, B. Yang, Y. Qian, H. Li, D. Gao, and L. Jiang, "Joint SOH and RUL estimation for lithium-ion batteries via optimal deep belief network with Bayesian algorithm," *J. Energy Storage*, vol. 131, p. 115891, Apr. 2025, doi: 10.1016/j.est.2025.115891.

[46] J. Zhao, X. Han, Y. Wu, Z. Wang, and A. F. Burke, "Opportunities and challenges in transformer neural networks for battery state estimation: Charge, health, lifetime, and safety," *J. Energy Chem.*, vol. 102, pp. 463–496, Mar. 2025, doi: 10.1016/j.jechem.2024.11.011.

[47] K. Zhang and X. Wang, "Joint Estimation of Lithium-Ion Battery Health Status and Remaining Service Life by Transfer Learning Based on PatchTST and Dynamic Weighted MSE Loss Function," *Energy Sci. Eng.*, vol. 13, no. 9, pp. 4371–4386, Sept. 2025, doi: 10.1002/ese3.70177.

[48] X. Yu, Z. Ma, and J. Wen, "Joint estimation of SOH and RUL for lithium batteries based on variable frequency and model integration," *Int. J. Electrochem. Sci.*, vol. 19, no. 11, p. 100842, Nov. 2024, doi: 10.1016/j.ijoes.2024.100842.

[49] C. Zhang *et al.*, "Battery SOH estimation method based on gradual decreasing current, double correlation analysis and GRU," *Green Energy Intell. Transp.*, vol. 2, no. 5, p. 100108, Oct. 2023, doi: 10.1016/j.geits.2023.100108.

[50] S.-Y. Shih, F.-K. Sun, and H. Lee, "Temporal pattern attention for multivariate time series forecasting," *Mach. Learn.*, vol. 108, no. 8–9, pp. 1421–1441, Sept. 2019, doi: 10.1007/s10994-019-05815-0.

[51] J. Huang *et al.*, "A lithium-ion battery SOH estimation method based on temporal pattern attention mechanism and CNN-LSTM model," *Comput. Electr. Eng.*, vol. 122, p. 109930, Mar. 2025, doi: 10.1016/j.compeleceng.2024.109930.

[52] W. He, N. Williard, M. Osterman, and M. Pecht, "Prognostics of lithium-ion batteries based on Dempster–Shafer theory and the Bayesian Monte Carlo method," *J. Power Sources*, vol. 196, no. 23, pp. 10314–10321, Dec. 2011, doi: 10.1016/j.jpowsour.2011.08.040.

[53] B. Saha and K. Goebel, "Prognostics Center of Excellence Data Set Repository - NASA," Battery Dataset. [Online]. Available: https://www.nasa.gov/intelligent-systems-division/discovery-and-systems-health/pcoe/pcoe-data-set-repository/

[54] P. M. Attia *et al.*, "Closed-loop optimization of fast-charging protocols for batteries with machine learning," *Nature*, vol. 578, no. 7795, pp. 397–402, Feb. 2020, doi: 10.1038/s41586-020-1994-5.

[55] F. Wang, Z. Zhai, B. Liu, S. Zheng, Z. Zhao, and X. Chen, "Open access dataset, code library and benchmarking deep learning approaches for state-of-health estimation of lithium-ion batteries," *J. Energy Storage*, vol. 77, p. 109884, Jan. 2024, doi: 10.1016/j.est.2023.109884.

论文中期考核 评议小组成员 MEMBERS OF EVALUATION TEAM	

论文评议小组对中期考核报告的意见（包括论文的进度、学术水平、成果、存在问题等，作扼要记录）：
COMMENTS OF EVALUATION TEAM ON THE MID-TERM REPORT (Including the progress of the dissertation, academic level, results, problems, etc.)

论文中期考核 评议小组成员 MEMBERS OF EVALUATION TEAM	陈杨　　赵闻　　吾而楷

论文评议小组对中期考核报告的意见（包括论文的进度、学术水平、成果、存在问题等，作扼要记录）：
COMMENTS OF EVALUATION TEAM ON THE MID-TERM REPORT (Including the progress of the dissertation, academic level, results, problems, etc.)

1. Strengthen experimental validation: Expand sample sizes, add control groups where applicable, and ensure your methodology is rigorous enough to support your core arguments.
2. Validate theoretical findings through empirical evidence—align your experiments closely with theoretical hypotheses to reinforce the credibility and persuasiveness of your research.

	序号 No.	论文名称 Title of Paper	刊物名称、卷（期）或会议名称、地点 Journal Name, Volume (Issue) or Conference Name, Place （著作及出版社 Books and Publishers）	排名 Individual Rankings
发表论文目录 Published Papers	1	Battery Prognostics and Health Management Using CNN-BiGRU with Temporal Attention on CS2 Cells	2025 Global Reliability and Prognostics and Health Management (PHM–Xi'an)	
	2			
	3			
	4			
	5			

	序号 No.	成果名称 Title of Achievement	获奖级别 Awards Level （国家、省、部、其他） National, provincial, ministry, and other	排名 Individual Rankings
科研成果目录 Research Achievements	1	Outstanding quality, clarity of presentation, and a significant contribution to the discourse of the3rd Belt and Road Academic Forum at Northwestern Polytechnical University.	Second Prize in the Poster presentation of scholarly articles	
	2			
	3			
	4			

发表论著综合统计（含审稿通过数）
The number of published works (Including the accepted papers)

论著合计（篇） Total	刊物发表（篇） Journal	会议宣读（篇） Conference	待发表（篇） To be published	专著（册） Monograph	EI、SCI、ISTP索引（篇） Index
1		1			

评议小组 意见 COMMENTS OF EVALUATION TEAM	1．论文进度： Progress:	☐超过计划 Exceed	☐符合计划 Accord	☐滞后计划 Lag	
	2．研究工作量： Workload:	☐饱满 Big	☐一般 Medium	☐偏少 Small	
	3．研究成果： Achievement：	☐显著 Remarkable	☐一般 Medium	☐太少 Less	
	4．独立科研工作能力： Research Ability:	☐良好 Good	☐较好 Above average	☐一般 Average	☐较差 Low
	5．总体评价： Overall evaluation:	☐很好 Excellent	☐良好 Good	☐合格 Qualified	☐不合格 Unqualified

评议小组 建议 SUGGESTION OF EVALUATION TEAM	

评议小组 意见 COMMENTS OF EVALUATION TEAM	1．论文进度： Progress:	☐超过计划 Exceed	☑符合计划 Accord	☐滞后计划 Lag	
	2．研究工作量： Workload:	☐饱满 Big	☑一般 Medium	☐偏少 Small	
	3．研究成果： Achievement：	☐显著 Remarkable	☑一般 Medium	☐太少 Less	
	4．独立科研工作能力： Research Ability:	☐良好 Good	☑较好 Above average	☐一般 Average	☐较差 Low
	5．总体评价： Overall evaluation:	☐很好 Excellent	☑良好 Good	☐合格 Qualified	☐不合格 Unqualified

评议小组 建议 SUGGESTION OF EVALUATION TEAM

As we reach the midpoint of your program, I wanted to share key reminders to keep your progress on track:
Prioritize submitting your research to academic journals promptly—timely publication is crucial for your program requirements and academic profile.
1.Stay focused and don't hesitate to reach out if you need guidance on manuscript preparation or English writing refinement.

备注 RESERVATION

备注 RESERVATION	